Bulletin of the Seismological Society of America, Vol. 103, No. 4, pp. 2305–2325, August 2013, doi: 10.1785/0120120303

Crustal Structure and Fault Geometry of the 2010 Haiti Earthquake from Temporary Seismometer Deployments

by Roby Douilly, Jennifer S. Haase, William L. Ellsworth, Marie-Paule Bouin, Eric Calais, Steeve J. Symithe, John G. Armbruster, Bernard Mercier de Lépinay, Anne Deschamps, Saint-Louis Mildor, Mark E. Meremonte, and Susan E. Hough

Abstract Haiti has been the locus of a number of large and damaging historical earthquakes. The recent 12 January 2010 M_w 7.0 earthquake affected cities that were largely unprepared, which resulted in tremendous losses. It was initially assumed that the earthquake ruptured the Enriquillo Plantain Garden fault (EPGF), a major active structure in southern Haiti, known from geodetic measurements and its geomorphic expression to be capable of producing M 7 or larger earthquakes. Global Positioning Systems (GPS) and Interferometric Synthetic Aperture Radar (InSAR) data, however, showed that the event ruptured a previously unmapped fault, the Léogâne fault, a north-dipping oblique transpressional fault located immediately north of the EPGF. Following the earthquake, several groups installed temporary seismic stations to record aftershocks, including ocean-bottom seismometers on either side of the EPGF. We use data from the complete set of stations deployed after the event, on land and offshore, to relocate all aftershocks from 10 February to 24 June 2010, determine a 1D regional crustal velocity model, and calculate focal mechanisms. The aftershock locations from the combined dataset clearly delineate the Léogâne fault, with a geometry close to that inferred from geodetic data. Its strike and dip closely agree with the global centroid moment tensor solution of the mainshock but with a steeper dip than inferred from previous finite fault inversions. The aftershocks also delineate a structure with shallower southward dip offshore and to the west of the rupture zone, which could indicate triggered seismicity on the offshore Trois Baies reverse fault. We use first-motion focal mechanisms to clarify the relationship of the fault geometry to the triggered aftershocks.

Online Material: Tables of hypocenter locations and focal mechanisms, and Figure showing azimuthal variation with respect to travel-time residuals.

Introduction

Hispaniola lies along the boundary between the North American and Caribbean plates. From east to west across Hispaniola, the plate boundary transitions from predominantly a subduction to a transform boundary (Calais *et al.*, 2002; Mann *et al.*, 2002). Geodetic studies (i.e., DeMets *et al.*, 1994) show that the Caribbean plate moves eastward at about 20 mm/year with respect to the North American plate. In the northeastern Caribbean this motion is partitioned between two thrust faults, the North Hispaniola fault (NHF) and the Muertos fault (MT), and two major strike-slip faults, the Septentrional fault (SF) and the Enriquillo Plantain Garden fault (EPGF). The Septentrional fault is assumed to have ruptured in 1842 (M 7.7–8.0) and 1887, whereas the EPGF is assumed to be responsible for the $M > 7$ 1751 and 1770 events (Ali *et al.*, 2008; Bakun *et al.*, 2012; Fig. 1). Historical seismicity in Hispaniola, combined with strain accumulation rates on active faults estimated from Global Positioning Systems (GPS) measurements, led Manaker *et al.* (2008) to conclude that sufficient strain had accrued across the Enriquillo Plantain Garden fault zone to generate an earthquake as large as M_w 7.2. The occurrence of an earthquake such as the devastating 12 January 2010 M_w 7.0 Haiti event was, therefore, anticipated. New probabilistic seismic hazard maps have been published that now take into account strain accumulation on the major faults (Frankel *et al.*, 2011) as well as historical and recent seismicity. The 2010 event was shallow, with an epicenter close to the trace of the Enriquillo fault and a centroid moment tensor (CMT) mechanism showing

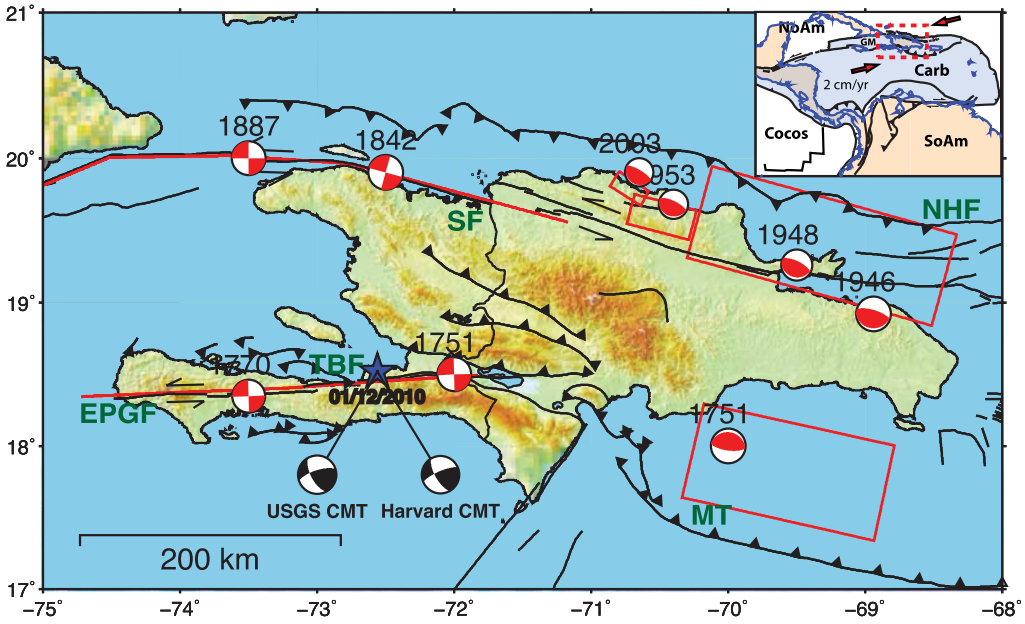

Figure 1. Historical earthquakes beneath Hispaniola and the surface projection of their assumed rupture planes. The red focal mechanisms for the historical earthquakes are assumed based on the tectonic setting. The Harvard and USGS CMT focal mechanisms for the 12 January 2010 earthquake are shown in black. North Hispaniola fault, NHF; Enriquillo Plantain Garden fault, EPGF; Trois Baies fault, TBF; Septentrional fault, SF; Muertos trough, MT (modified from Ali *et al.*, 2008). Inset: Location of the Caribbean plate (CARB) and the island of Hispaniola (red dashed box; North American plate, NoAm; South American plate, SoAm; Gonave microplate, GM); orientation and rate of relative motion between Carb and NoAm, arrows.

primarily strike-slip motion, with a small component of reverse motion, on a steeply north-dipping nodal plane (Nettles and Hjörleifsdóttir, 2010).

The earthquake prompted several field experiments as well as Interferometric Synthetic Aperture Radar (InSAR) data acquisitions, including the deployment of on-land seismic stations and ocean-bottom seismometers (OBS; Altidor *et al.*, 2010; de Lépinay *et al.*, 2011) to precisely locate aftershocks, record ground motions, and gain insight into the coseismic rupture mechanism and geometry of the EPGF zone. The aftershock locations available from the National Earthquake Information Center (Fig. 2) were not sufficiently precise to delineate the rupture geometry. Nettles and Hjörleifsdóttir (2010) used data from regional seismic stations to show that $M > 5$ aftershocks during the month following the main event were located mostly at the western end of the event rupture with, surprisingly, pure reverse-faulting mechanisms. Based on an inversion of coseismic offsets from GPS and InSAR data, and an absence of significant surface rupture, Calais *et al.* (2010) argued that the earthquake did not rupture the Enriquillo fault but rather ruptured an unmapped fault dipping roughly 60° to the north. The fault was named the Léogâne fault, as it was clearly distinguishable from the strike-slip Enriquillo fault, which is assumed to be vertical to south dipping in this area based on its geomorphic expression (Prentice *et al.*, 2010). The geodetic inversion showed that coseismic slip involved two-thirds left-lateral strike-slip motion and one-third reverse dip-slip motion. Hayes *et al.* (2010) performed a similar inversion, which also included seismic and coastal uplift data. They suggested that the rupture initiated on the Enriquillo fault, then transferred to the Léogâne fault, where the large majority of moment release occurred. They argue for a third, south-dipping rupture segment to the east of the Léogâne fault. Such a complex rupture geometry raises questions about the relation between the slip during the Haiti earthquake and the geometry and tectonic history of the mapped geologic faults.

de Lépinay *et al.* (2011) used OBS and several land seismic stations to relocate the early aftershocks, which they found to align in a direction slightly oblique to, and to the north of, the Enriquillo fault. They argued that the compressional component of motion during the earthquake was consistent with the evidence of longer-term oblique collision between Haiti's southern peninsula and the rest of Hispaniola island seen in the Haitian fold-and-thrust belt (Pubellier *et al.*, 2000). Recently Meng *et al.* (2012) used a backprojection technique to show that the energy generated in the mainshock originated from two separate subevents. They also performed a slip inversion using seismic, InSAR, GPS, and coastal uplift data and inferred that the rupture occurred on two faults: the Léogâne fault to the east and a distinct north-dipping fault to the west that they incorrectly associated with the Trois Baies fault, which is, in fact, south dipping.

In this work we use data from the complete set of seismic stations deployed in southern Haiti after the 12 January earthquake, both on land and offshore, together with high-resolution earthquake location techniques to relocate aftershocks that occurred from 10 February to 24 June 2010.

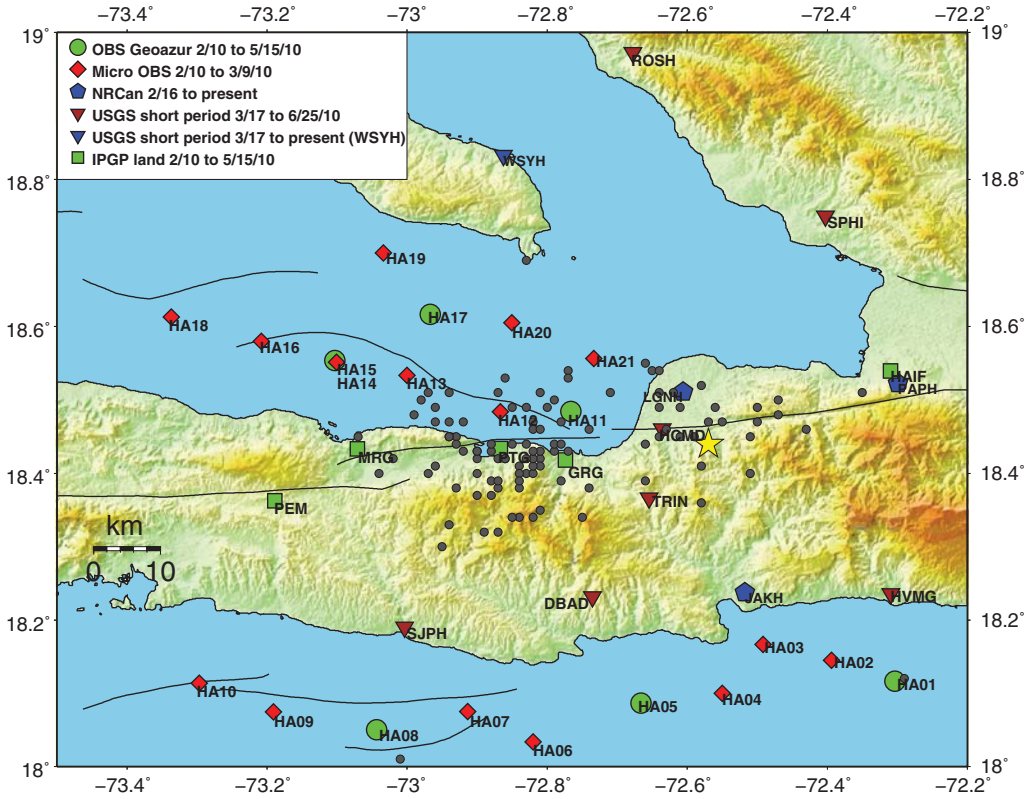

Figure 2. Seismic stations include 15 short-period microOBS, 6 broadband OBS, 7 broadband land stations, and 9 co-located short-period and strong-motion stations that were installed after the mainshock. These stations, except the strong-motion stations, were used to locate the aftershocks and determine the crustal velocity structure. Position of the mainshock, yellow star; aftershock locations according to the National Earthquake Information Center (NEIC) catalog, gray dots; previously mapped fault trace, thin lines.

Although the relationship between aftershock locations and mainshock ruptures can be complex (Mendoza and Hartzell, 1988), many studies have concluded that aftershocks generally illuminate mainshock rupture planes (e.g., Ratchkovski *et al.*, 2004). The spatial distribution of aftershock sequences can migrate with time, consistent with predictions of an Epidemic Type Aftershock Sequence model (e.g., Helmstetter and Sornette, 2002). Early aftershocks might thus delineate a mainshock rupture better than later events. In this case, the first stations were not deployed until four weeks after the mainshock. Thus, although relocated aftershock locations can be useful to better illuminate the fault(s) that participated in the mainshock, the distribution will almost certainly also reflect activation of secondary faults in addition to the primary mainshock rupture. One key question, therefore, will be the extent to which relocated aftershocks delineate clear planes that are consistent with independent constraints for the mainshock rupture geometry.

Seismological Data

Prior to the 12 January mainshock, no research-quality seismic stations were operating in Haiti. Beginning on 10 February 2010, research groups from the French laboratory Géoazur and the Institut Français de Recherche pour l'Exploitation de la Mer (IFREMER) installed two types of OBS offshore the southern peninsula (Fig. 2; de Lépinay *et al.*, 2011). Fifteen microOBS (short-period sensors and hydrophone) from IFREMER, which can record for three weeks, operated through 9 and 10 March 2010, and six broadband OBS "Seahorse" instruments from Géoazur, which can record for up to three months, operated through 15 and 16 May 2010. All the OBS have four components, including a 2 Hz hydrophone (de Lépinay *et al.*, 2011). During the same period, the Institut de Physique du Globe de Paris (IPGP) operated four broadband seismometers with collocated accelerometers near the Enriquillo fault. We use also one short-period velocity station in Port-au-Prince from Sismos à l'école (Courboulex *et al.*, 2012). On 16 February 2010, the Natural Resources Canada (NRCan) agency installed three broadband seismic stations at Jacmel, Léogâne, and Port-au-Prince (Fig. 2). Finally, in March 2010, eight short-period stations (three-component L-22 sensors with Reftek recorders) and nine strong-motion seismometers (Kinemetrics K2s with FBAs and, at two stations, short-period vertical sensors) were installed by the U.S. Geological Survey (USGS) and the Haiti Bureau of Mines and Energy (BME) in the Port-au-Prince area (Altidor *et al.*, 2010; Hough *et al.*, 2010).

In this study, we analyze data recorded by the short-period and broadband stations but not the strong-motion instruments. The combined set of stations (Fig. 2 and Table 1)

Table 1
Seismic Station Information with their Delay Time Corrections Determined Jointly with the 1D Velocity Model

Station Name	Latitude (° N)	Longitude (° W)	Elevation (km)	*P*-Wave Station Correction (s)	*S*-Wave Station Correction (s)	Date Installed (yyyy/mm/dd)	Date Recovered (yyyy/mm/dd)	Network Name
DBAD	18.2315	72.73536	0.534	0.10	0.44	2010/03/15	2010/06/25	USGS
HCMD	18.4606	72.65593	0.074	0.00	0.56	2010/03/13	2010/06/25	
HVMG	18.2357	72.30294	0.145	−0.27	−0.27	2010/03/16	2010/06/24	
ROSH	18.9725	72.67772	0.139	−0.45	−0.57	2010/03/09	2010/06/24	
SJPH	18.1903	73.00340	0.022	0.15	0.51	2010/03/16	2010/06/22	
SPHI	18.7501	72.40264	0.101	−0.25	−0.22	2010/03/11	2010/06/21	
TRIN	18.3662	72.65462	0.334	0.11	0.54	2010/03/17	2010/06/25	
WSYH	18.833	72.86274	0.029	−0.35	−0.48	2010/03/10	—	
JAKH	18.2377	72.5180	0.047	0.16	0.63	2010/02/16	—	NRCAN
LGNH	18.5110	72.6058	0.062	−0.05	0.15	2010/02/14	—	
PAPH	18.5225	72.2993	0.218	0.00	0.34	2010/02/11	—	
PEM	18.3627	73.1888	0.29	0.02	0.27	2010/02/10	2010/05/15	IPGP
MRG	18.4335	73.0712	0.05	−0.01	0.23	2010/02/10	2010/05/15	
PTG	18.4338	72.8668	0.01	0.11	0.57	2010/02/10	2010/05/15	
GRG	18.4182	72.7738	0.04	0.11	0.45	2010/02/10	2010/05/15	
HAIF	18.5395	72.3097	0.15	0.03	0.40	2010/02/10	2010/05/15	Sismo-Ecole
HA01	18.1167	72.3037	−3.85	−0.09	0.72	2010/02/10	2010/05/15	GEOAZUR (BBOBS)
HA05	18.0503	72.6663	−1.98	0.24	1.18	2010/02/10	2010/05/15	
HA11	18.4843	72.766	−1.09	−0.01	0.75	2010/02/10	2010/05/15	
HA14	18.5538	73.1033	−1.55	0.58	1.70	2010/02/10	2010/05/15	
HA17	18.6167	72.9672	−1.51	0.09	1.04	2010/02/10	2010/05/15	
HA02	18.145	72.3938	−2.71	−0.04	1.15	2010/02/10	2010/03/09	IFREMER (micro-OBS)
HA03	18.1667	72.4917	−0.46	0.03	1.03	2010/02/10	2010/03/09	
HA04	18.1	72.5498	−2.4	0.26	1.18	2010/02/10	2010/03/09	
HA06	18.0337	72.8203	−1.64	0.32	1.23	2010/02/10	2010/03/09	
HA07	18.0752	72.9135	−1.13	0.27	1.02	2010/02/10	2010/03/09	
HA09	18.0747	73.191	−1.16	0.03	0.73	2010/02/10	2010/03/09	
HA10	18.1137	73.297	−1.43	0.12	1.03	2010/02/10	2010/03/09	
HA13	18.5338	73.0002	−1.65	0.25	1.31	2010/02/10	2010/03/09	
HA15	18.5517	73.1008	−1.55	0.38	1.53	2010/02/10	2010/03/09	
HA16	18.58	73.2082	−1.31	0.23	1.54	2010/02/10	2010/03/09	
HA18	18.6132	73.3367	−1.59	0.27	1.07	2010/02/10	2010/03/09	
HA19	18.7003	73.0337	−1.04	−0.12	0.48	2010/02/10	2010/03/09	
HA20	18.6052	72.8507	−0.83	0.12	0.75	2010/02/10	2010/03/09	
HA21	18.5565	72.7335	−0.67	0.06	0.74	2010/02/10	2010/03/09	

is available to locate the aftershocks and develop a crustal velocity model for the area. The station elevations ranged from 534 m above sea level to −3.85 km for the deepest OBS. We analyze all available data from 10 February to 24 June 2010. The land station timing was controlled by GPS with synchronization every hour providing timing accuracy of ∼3 ms, which is less than the picking errors. For the microOBS, the three weeks time drift was <50 ms, and we induce an estimated accuracy of the timing better than 10 ms, after correcting for clock drift. For the long-term OBS, the estimated accuracy can be estimated from the mean time drift measurements to 100 ms. The arrival times were picked using the Seismic Analysis Code (Goldstein *et al.*, 2003), and quality checks were done to down-weight or remove arrivals that were found to have anomalously large residuals. All of the data have a sampling rate of 100 sample/sec and the picks were assigned a quality indicator of 0, 1, 2, and 3 based on their estimated picking error of 0.02, 0.04, 0.06, and 0.08 s, respectively. In the VELEST implementation, these picks were given relative weights of 1, 1/4, 1/16, and 1/64. OBS *P*-wave arrivals were picked off the hydrophone channel, which showed much clearer arrivals. *S*-wave arrivals were picked on the most impulsive of the two horizontal components for land and OBS stations. *S* arrivals were assigned uncertainties using the same quality scale, so the majority of the picks were quality 3. We included only data in the inversion that, after an initial quality check, had *P*-wave residuals <1 s and *S*-wave residuals <1.5 s. For some events, particularly for OBS station HA01, we sometimes noticed late *P*-wave arrivals, which led to a bimodal distribution in the residuals. These late arrivals might be converted phases from deeper layers, so they were given lower weight. The final dataset included 10,503 *P*-wave arrivals and 10,187 *S*-wave arrivals for a total of 1274 events.

Simultaneous Velocity, Station Correction, and Hypocenter Inversion

Starting Velocity Model Determination

P- and *S*-wave arrivals from all the stations, except the strong-motion stations, were compiled to locate the after-

shocks and develop a crustal velocity model for the area. We used the VELEST program (Kissling *et al.*, 1995) to simultaneously invert for *P*- and *S*-wave 1D velocity models, station corrections, and earthquake locations (Crosson, 1976; Kissling, 1988; Kissling *et al.*, 1994, 1995). The method applies velocity damping as regularization to find the minimum velocity change from the starting model for poorly constrained layers. The method outlined by Kissling *et al.* (1994) emphasizes using the smallest number of layers that is required, to help convergence in this iterative approach. This limits our ability to determine independently exact depths of the interfaces between velocity layers. The method is successful, however, in finding a best-fitting velocity model given the specified layer depths. We used several iterations of the inversion process to test different hypotheses for the velocity model. Previous studies in the Caribbean region provide estimates of crustal structure and properties. We use these studies to guide the choice of a starting model. Wiggins-Grandison (2004) solved for 1D *P*- and *S*-velocity models for the Jamaican crust and upper mantle. She modeled the crust as four layers with velocities of 5.15 km/s at 0 km below sea level, 6.30 km/s at 4.5 km depth, 6.60 km/s at 9 km, 7.11 km/s at 22 km, and 7.81 km/s at 30 km. Similar studies were done in Puerto Rico (Murphy and McCann, 1979) and southern Cuba (Moreno *et al.*, 2002); these studies, however, only inverted for *P*-wave velocity.

Because the results of the nonlinear inversion may be sensitive to the initial parameters, we tested the variability of the convergence of the solution with respect to each of these regional starting velocity models in the following manner. We selected the 720 events from 21 February to 20 April 2010 that had the most arrivals per event, with 8291 *P*-wave arrivals and 6458 *S*-wave arrivals. Each event had at least 8 *P* arrivals and 2 *S* arrivals, and the average was 15 *P* arrivals and 10 *S* arrivals per event. This time period corresponds to the time period when OBSs were deployed and also corresponds to the dataset with the best geometrical distribution, in particular, with an average azimuthal gap of 115°. We solved for the *P*-wave velocity model without station corrections. *S*-wave arrivals were included in the hypocenter locations with *S*-wave velocity constrained by a V_P/V_S ratio of 1.75. We did not, however, solve for *S*-wave velocity at this step. This ratio was chosen based on the slope of the Wadati diagrams, which gave V_P/V_S that varied from 1.69 to 1.85. We modified the layer depths of the three different *P*-wave starting models (Jamaica, southern Cuba, and Puerto Rico), which have different layer thicknesses and different velocities, to allow the velocity to change at the depths of −1, 4, 5, 7, 9, 12, 20, 22, and 30 km below sea level for all three models (Fig. 3a). Then we determined three refined estimates of the regional model based on our dataset with three separate VELEST runs. We set a damping value of 0.01 for the earthquake hypocenters and origin times (Kissling *et al.*, 1995) and a damping of 0.50 for the velocities (a damping value of ~1000 will fix the model parameters to the initial values).

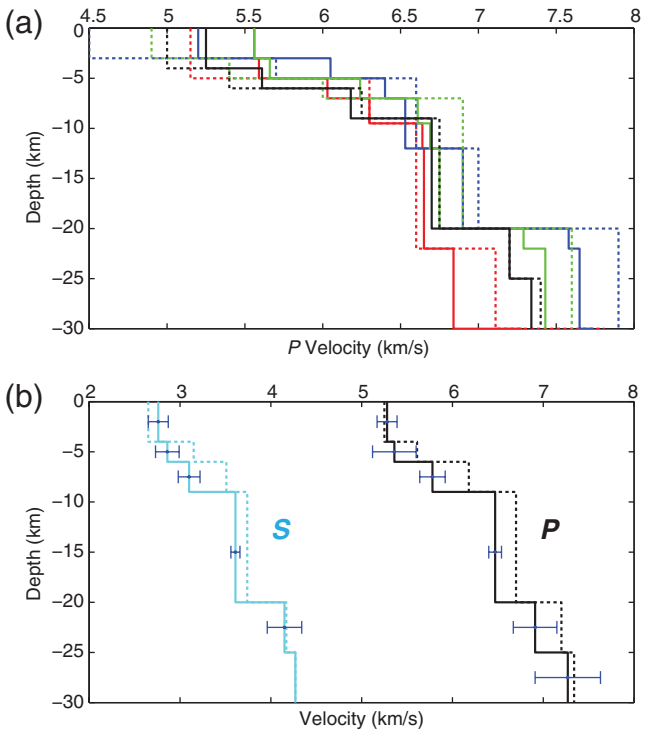

Figure 3. 1D velocity profiles. (a) Initial *P*-wave velocity models (dashed line) and final models (solid line) from several runs of the the simultaneous inversion without station corrections. The initial models are taken from seismic studies in Jamaica (red line; Wiggins-Grandison, 2004); Puerto Rico (blue line; Murphy and McCann, 1979); and southern Cuba (green line; Moreno *et al.*, 2002). The average of the three resulting velocity models, black dashed line; best 1D model without station corrections, solid black line. (b) The best 1D model (dashed line) without station corrections, which is used for the initial model in the inversion for the final 1D model with station corrections (solid line). The horizontal blue lines are the error bars. We do not reliably determine the Moho depth because there are not enough rays that sampled the deeper layers, and the *S*-wave velocity uncertainty in the deepest layer is unknown.

The elevation difference between the deepest OBS and the highest land station is 4.38 km. This elevation difference affected our parameterization of the shallow velocity structure, as VELEST ray traces to the elevation of the stations and requires that all stations be confined in the first layer to invert for station corrections in later steps. The lateral velocity variations in this first layer are expected to be large, and station corrections will only account for this to first order. Relative locations will ultimately provide the best compensation for variations in shallow structure. In Figure 3b, zero is at sea level, and the model extends to a depth of 30 km. The Jamaica, southern Cuba, and Puerto Rico models had a starting root mean square (rms) of 0.43, 0.48, and 0.47 s and an ending rms of 0.18, 0.19, and 0.20 s, respectively. Small differences of <0.3 km/s were found with the three different starting models. The implementation of the velocity damping in the inversion (Kissling, 1988) limits the variation from the

initial starting model; the inversions, however, were iterated >10 times until the velocities varied by <0.1 km/s. Therefore, we believe it was not the damping that limited convergence, but it was likely that the three varying results represent local minima in the objective function. Solving for V_S explicitly might be expected to allow the inversion to reach a global minimum, which was attempted in the following step. The average *P*-wave slowness was calculated from these three resulting estimates, and the initial value of 1.75 was used for the V_P/V_S ratio in the next inversion without further constraint on the V_P/V_S ratio. The result of this inversion, also without station corrections, is shown by the black line in Figure 3a. This result has intermediate V_P values, a comparable misfit (rms of 0.18 s) to the inversions using the regional starting models, and least-squares velocity errors of 0.23 km/s in the layers above 20 km. Therefore, we proceed to an inversion including station corrections to determine whether lateral heterogeneity is a major cause of the data misfit.

Velocity Model and Station Corrections

We use the best-fitting velocity model without station corrections described above as the starting model along with the 720 selected events in a simultaneous inversion for the best-fitting velocity structure including station corrections and hypocenter locations, once again without constraint on the V_P/V_S ratio. The station corrections are parameterized relative to a reference station the *P*-wave correction of which is fixed to zero. We chose station HCMD to be the reference station because it has the most recordings and because it is centrally located. After investigating the effect of different relative damping for the velocity and station correction parameters we assigned damping values of 0.01, 0.01, 10, and 0.1 for the earthquake hypocenter, origin time, velocity, and station corrections, respectively (see Kissling *et al.*, 1994, for a discussion of the choice of these parameters). We iterated the solution, performing one iteration where only hypocenters were determined, alternating with one iteration where hypocenters, station corrections, and velocities were simultaneously determined. We continued iterations until the solution (hypocenter, station corrections, and crustal velocities) converged to a model where there were no further significant changes in velocity, hypocenter, and station corrections, that is, less than 0.03 km/s, 0.02 km, and 0.02 s change, respectively. This final velocity model has V_P/V_S ratio of ~1.8 in the best-constrained depth of 9–20 km, which is typical of mafic rocks in oceanic crust (Christensen, 1996). It is consistent with a substratum of the southern peninsula composed of cretaceous tholeitic basalts from the Caribbean oceanic basins (Momplaisir, 1986). Higher V_P/V_S in the shallower layers may be due to serpentinization of the crust or the presence of fluids (Christensen, 1996). We refer to this final model as the minimum 1D model (Figs. 3b, 4), and we located the entire dataset of 1274 events with the velocity and station corrections fixed to these values. The final result reduced the rms misfit from 0.18 s without station corrections to an rms misfit of 0.14 s with station corrections and gave a variance reduction of 46% (for a complete list of earthquake locations using VELEST, Ⓔ see Table S1 in the electronic supplement to this article).

We tested the convergence of the hypocenters to unique locations in the final model in the following manner. We shifted all the hypocenters by 15 km horizontally and 2 km vertically. Then we relocated the aftershocks with the velocity and station corrections fixed and compared the starting and ending locations. More than 80% of the hypocenters returned to within 600 m of their original locations. The rest of the events, primarily those located offshore in the western zone of the aftershock distribution after the time period when the OBSs were removed, have insignificant horizontal variations, but the depth variation is significant, which indicates that the depths of those events are not well constrained.

Moreno *et al.* (2002) show that the Moho discontinuity in southern Cuba in their average 1D model is 20 km deep. They included ray paths that traversed the thinner oceanic crust of the Gonave microplate (Mann *et al.*, 1991) between Cuba and Jamaica, as well as ray paths that were confined to sample only the thicker Cuban crust or the thicker Nicaragua rise of Cretaceous island arc material (Perfit and Heezen, 1978). Wiggins-Grandison (2004) found that the Moho in Jamaica is at 30 km depth, based on analysis of a dataset where ray paths were limited to the island of Jamaica. In both cases the increase in velocity found at the Moho was 0.7 km/s. In our model, we have specified layer interfaces at 20 and 25 km. The increase in velocity at 20 km depth is 0.51 km/s, and the increase in velocity at 25 km depth is 0.29 km/s. As only a few rays had passed through the layer between 20 and 25 km (196 rays), however, compared to the ray paths that travel through layers above, and as we did not include regional stations in the inversion, we do not have strong constraints on the Moho depth or velocity contrast. Further studies may provide better understanding of the depth of the Moho, for example, a receiver function analysis where the ambiguity between depth and velocity could be constrained with information from this study. A more detailed study of waveforms at regional distances to determine the attenuation structure (McNamara *et al.*, 2012) found a Moho depth of 20.6 km and an upper mantle velocity of 7.7 km/s from *Pn* arrivals, which is consistent with our results. The *P*- and *S*-wave arrival-time data at regional distances were not included in our study because they have much larger uncertainties and, therefore, would likely produce inconsistent locations between aftershocks that were recorded with OBS arrivals and those without OBS arrivals.

The *P*- and *S*-wave station corrections along with the final velocity model are provided in Tables 1 and 2. The deep OBS stations have relatively high *S*-wave station corrections (i.e., observed travel times are slow). The travel times are calculated to the elevation of the station, so large positive station corrections for the lowest stations are most likely due to thick layers of sediment accumulated in the ocean basins.

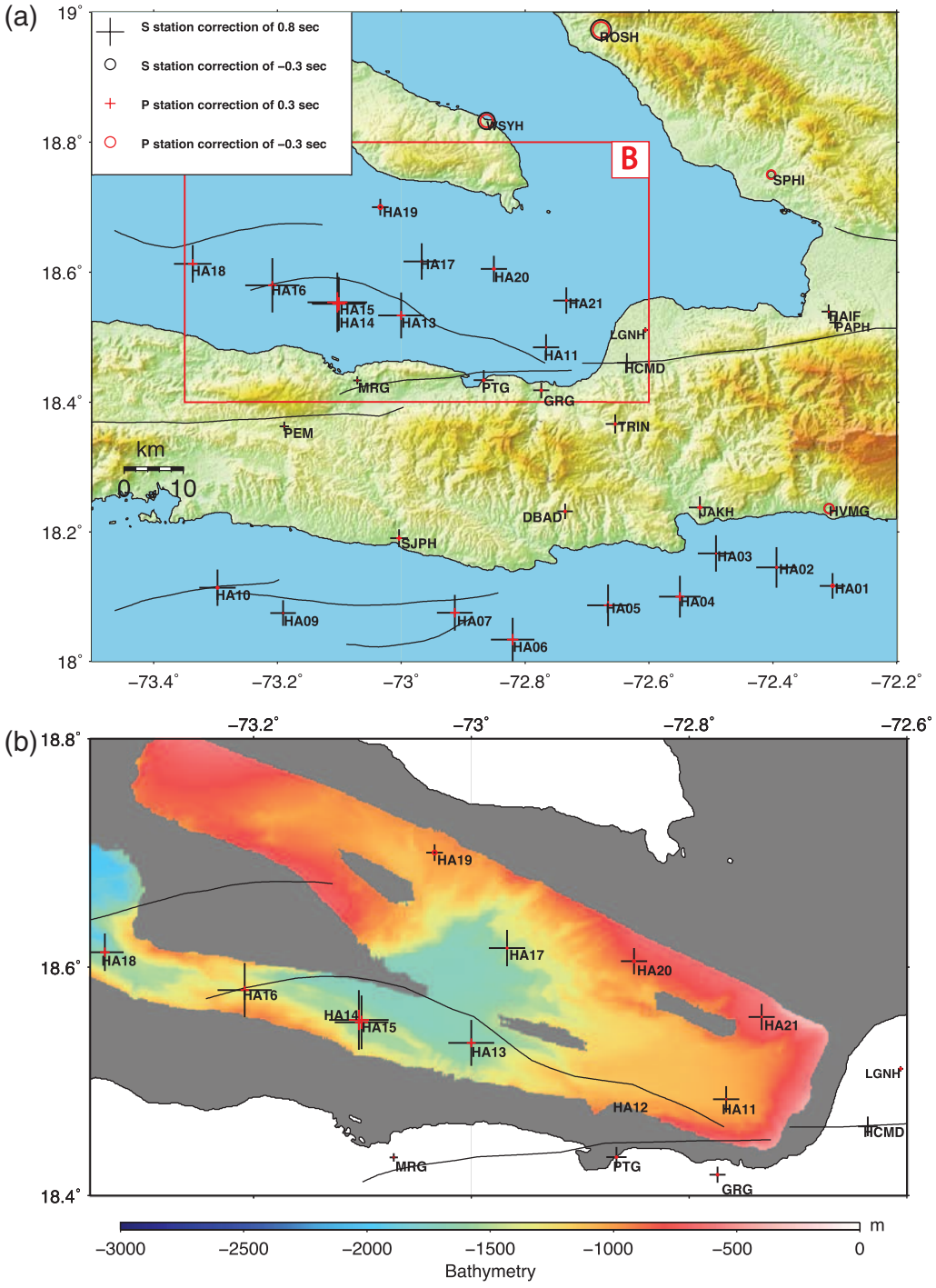

Figure 4. (a) Spatial distributions of *P*- and *S*-wave station corrections relative to site HCMD, which has a *P*-wave station correction fixed to zero. The variation of the station corrections for onshore versus offshore sites is evidence of velocity heterogeneity. (b) Details of the bathymetry north of the southern peninsula, along with the offshore station corrections. The OBS stations in deep sediment-filled basins have relatively high *S*-wave station corrections.

A marine survey of the offshore ocean basins provides an estimate of the thickness of the sediments (Momplaisir, 1986). The basins, with average depth below sea level of 1700 m, contain thick sequences of Plio-Quaternary sediments (Momplaisir, 1986). Two horizons were mapped from seismic profiles that correspond roughly to the top of the Eocene (D) and the base of the sedimentary sequence (F). The *S*-wave station corrections show a rough correlation with

Table 2
P and *S* Velocity for Best-Fitting 1D Model with Station Corrections

Depth (km)	*P* Velocity (km/s)	*S* Velocity (km/s)	V_P/V_S
0	5.28 ± 0.11	2.76 ± 0.11	1.91
4	5.36 ± 0.24	2.86 ± 0.13	1.87
6	5.78 ± 0.14	3.10 ± 0.12	1.86
9	6.50 ± 0.07	3.61 ± 0.05	1.80
20	7.01 ± 0.24	4.15 ± 0.19	1.69
25	7.30 ± 0.36	4.27–	1.71

the depth to horizon F (Fig. 5), as might be expected as sediment velocities would be expected to be lower for both *P*- and *S*-wave velocities.

There is interesting evidence for lateral variations in velocity, in addition to the station corrections. This is not surprising given the significant topographic differences in the southern peninsula and its offshore areas, as well as its complex tectonic history. The 1D model minimizes the travel times overall, but Figures 6 and 7 show some systematic trends in residuals for selected ray paths in the OBS and land stations, respectively. For sites located south of the aftershock distribution on the southern side of the peninsula and offshore (e.g., sites HA01, HA03, HA07, and JAKH), there is a positive trend to the residuals with distance indicating slower than average velocities for these paths (Fig. 6). For sites located offshore to the north of the rupture and many paths traveling parallel to the rupture toward eastern stations in the Port-au-Prince region, the residuals have a negative trend with distance indicating faster than average velocities in deeper layers (Fig. 7).

We examined the azimuthal variation of travel-time residuals as well. For most sites on land, the residuals show no variation with azimuth, which implies that the velocity is relatively homogeneous on land, and a layered 1D model may be a good approximation over most of the peninsula. Stations HA01, HA02, HA03, and HVMG, however, show particularly high residuals (observed times slower than modeled) for sources in the Trois Baies cluster of aftershocks, once again indicating slower velocities beneath the peninsula in a narrow azimuth range (Ⓔ see Fig. S1 in the electronic supplement). Unfortunately, the overall azimuthal distribution of data is poor, and the OBS instruments were not deployed for the entire time period. The offshore stations have a maximum azimuthal coverage of $< 80°$. This, combined with the fact that seismicity is confined to a limited area, would make it very difficult to unambiguously resolve lateral velocity variations, in particular making it difficult to reduce tradeoffs between the magnitude of the offshore velocity perturbations and their extent in the direction of the source to station.

Tomographic inversions should be considered in the future, if more data become available through long-term monitoring of sources in an extended geographic area, or through dedicated controlled source experiments (i.e., Hardebeck, 2010). Differences in lower crustal velocities beneath the peninsula and off the northern shore could also be investigated further using regional waveform modeling. The 1D model with station corrections is a useful approximation for providing refined earthquake locations because it produces zero mean residuals on average and accounts for first-order lateral variations. The residuals, however, show that lateral variations in velocity contribute to the misfit and explain why the rms of the final model remains greater than the picking error.

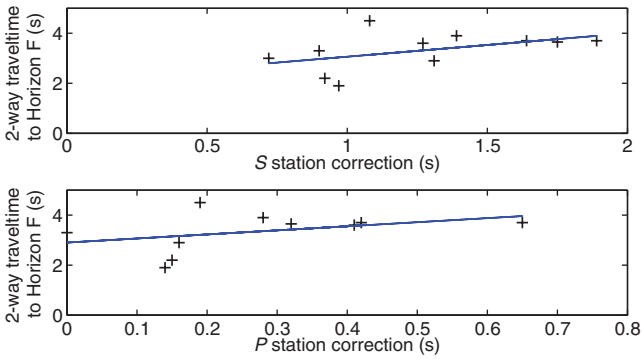

Figure 5. Two-way travel time from seismic profiles to horizon F, representing the base of the offshore sediments (Momplaisir, 1986) at the location of the OBS sites, as a function of the *S*-wave and *P*-wave station correction for each site.

Aftershock Relocation Using the Double-Difference Method

To further improve the aftershock locations, we employ a double-difference algorithm, which renders their spread less dependent on differences in the distribution of stations that recorded any given event (Waldhauser, 2001). The double-difference method can reduce relative location error for closely spaced events without the use of station corrections (Waldhauser and Ellsworth, 2000). This technique, commonly used to analyze events in dense aftershock zones where the distance between nearby aftershocks is < 1 km, links pairs of event neighbors through both *P*- and *S*-wave travel-time differences recorded at common stations and uses differentials of these travel-time differences to simultaneously solve for the offset of each event relative to the centroid of the event cluster (Waldhauser and Ellsworth, 2000).

The final 1D velocity model described in the Velocity Model and Station Corrections section is used for the relative earthquake relocations with HYPODD. This program works in a two-step process. First, HYPODD links the events and separates the data into different clusters based on the maximum separation. We fix the minimum number of observations per event pair to be eight and the maximum event separation to be 10 km. In this way, the isolated events are removed. During

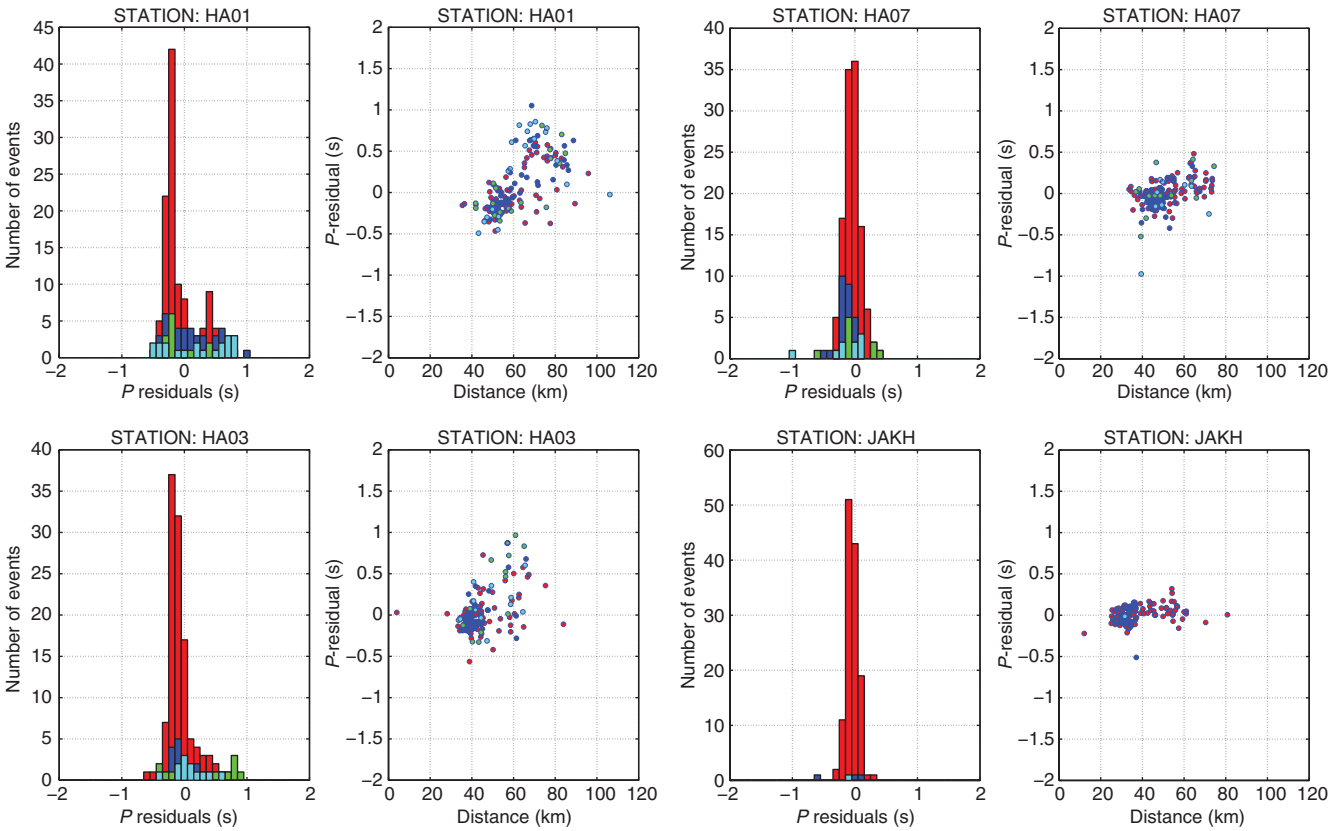

Figure 6. Distribution of the *P*-wave residuals for four stations with a positive trend to the residuals with distance. HA01, HA03, HA07, and JAKH are on the south side of the southern peninsula of Haiti. Red, blue, green, and cyan are quality indicators of 0, 1, 2, and 3, respectively, for the picks.

the next step, which is the inversion for coordinates, reweighting the data after each iteration can cause the event separations to change so that a small number of additional events exceeds the separation criterion and get removed. Events are also removed if their locations are perturbed above the surface (Waldhauser, 2001). Thus, the dimension of the design matrix for the inverse problem is reduced to 81%, and the number of events for which relative earthquake locations are determined is reduced to 1023 events (for a complete list of earthquake locations using HYPODD, Ⓔ see Table S2 in the supplement). The number of travel-time differences for pairs of earthquake is 76,587 for *P* waves and 50,841 for *S* waves. Only differences of observed travel times were used; no absolute travel times were used, nor were cross-correlated arrival times used. The absolute relocated hypocenters using the 1D velocity model with station corrections are shown in Figure 8, with the aftershock clusters that we refer to as zones A, B, and C shown in the corresponding cross sections A–A′, B–B′, and C–C′. These relocated hypocenters provide a vastly improved resolution of the fault geometry than the NEIC locations in Figure 2. The relative locations calculated using HYPODD in Figure 9 show even further improvement. For all events, there is a reduction of rms residuals from the absolute locations determined in the simultaneous velocity inversion with station corrections calculated with VELEST (rms of 0.14 s) compared to the relative locations calculated with HYPODD, which gives a final rms of 0.09 s. Any remaining misfit could be due to velocity variations within the length scale of the hypocenter clusters and would also contribute to the wider histograms seen in Figures 6 and 7. Velocity variations at this scale would not be easily removed by double differencing.

The system of double-differenced equations can be solved with two methods: conjugate gradient (LSQR; Fig. 9) and single value decomposition (SVD). SVD can be used to relocate small systems (~200 events), but LSQR is more efficient for larger datasets. Unfortunately, model parameter errors reported by LSQR are known to be underestimated (Paige and Saunders, 1982; Waldhauser and Ellsworth, 2000). For this reason, to determine the accuracy of the hypocenters, we subdivide the dataset into smaller groups of 200 events and relocate each group separately using SVD, which led to a total of 923 events. The hypocentral depth error is shown in Figure 10. The depth error is greater, ~4 km, for the LSQR events deeper than 12 km in cluster A. The median horizontal error for all events is ~400 m, and the average depth error excluding the deep events in

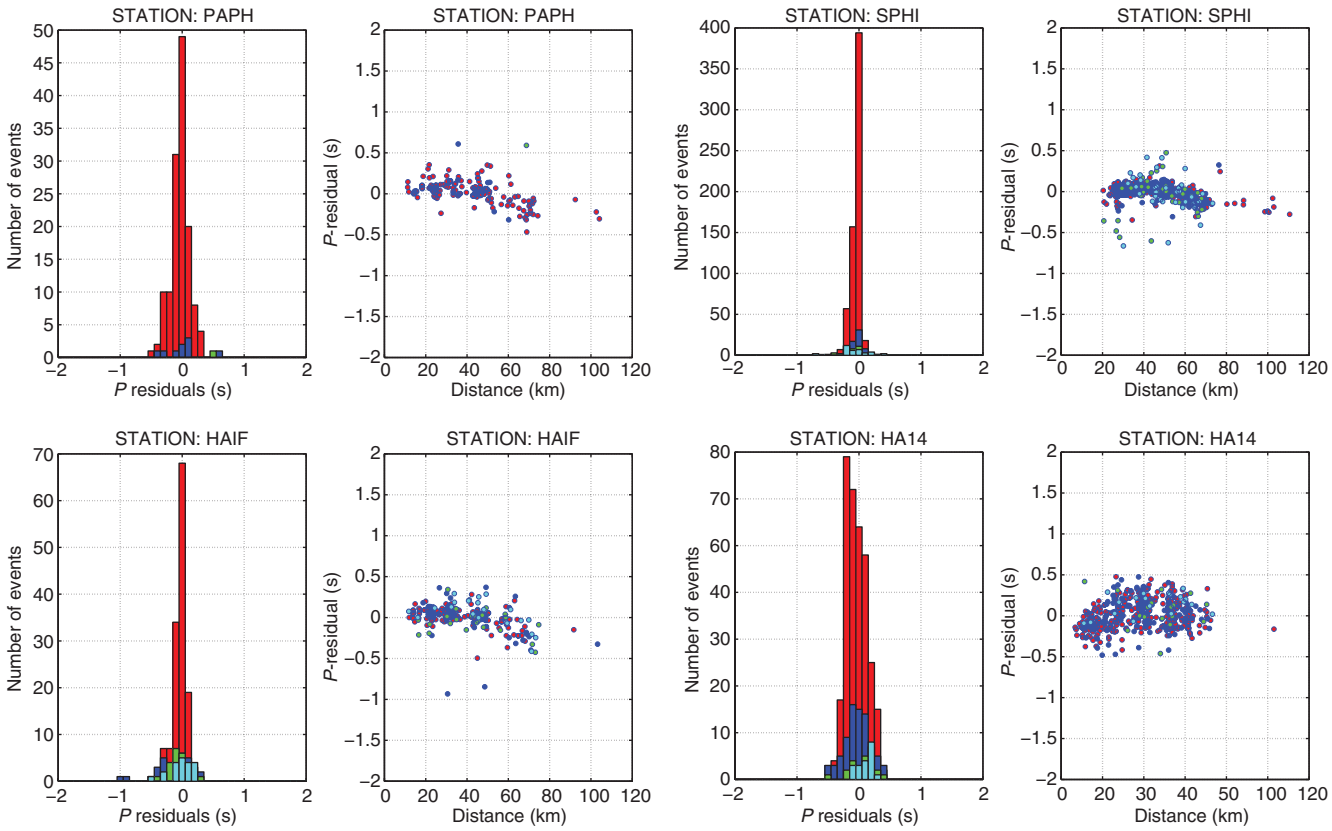

Figure 7. Distribution of the *P*-wave residuals for four stations with a negative trend to the residuals with distance. HAIF, PAPH, SPHI, and HA14 are located in the north side of the southern peninsula of Haiti. Red, blue, green, and cyan are quality indicators of 0, 1, 2, and 3, respectively, for the picks.

cluster A is ∼1 km. Each hypocenter obtained from the SVD method is compared to their corresponding LSQR solution to ensure consistency in the relocations. All event locations are stable except for a few events in cluster C and the deep events from cluster A (Fig. 11; blue events in cross section A–A′).

In summary, we have used three approaches to investigate the uncertainty in the depth of the hypocenters: estimating the formal errors in the absolute hypocentral location least-squares inversion (median horizontal error of ∼400 m and average depth error of ∼1 km), displacing the hypocenters and relocating to determine the stability of the locations, and comparing the results using SVD and LSQR in the relative location run that signals events with poorly constrained depth. The three approaches all indicate that the depths of events below 12 km in the Trois Baies cluster A–A′ in Figure 9 are poorly constrained and the uncertainties for these events are probably underestimated. Events in cluster A located below 12 km depth occurred almost exclusively from mid-March to late June after the micro-OBS had been removed. This resulted in a gap in the station distribution; therefore, the depths of deeper events are not as well constrained as the rest of the aftershock catalog.

First-Motion Focal Mechanisms

By using the final catalog of HYPODD locations described above, we compute *P*-wave first-motion focal mechanisms using the least-squares grid search software FPFIT (Reasenberg *et al.*, 1985) to find the best double-couple fault-plane solutions. A misfit value is calculated for each fault-plane solution, which is defined as the number of inconsistent polarity observations weighted by the observation quality and distance from the nodal planes. This misfit varies from 0.0 to 1.0, where 0.0 represents a perfect fit to the data (Reasenberg *et al.*, 1985). To obtain a reliable set of focal mechanisms we choose the events that meet the following criteria: a minimum of 13 *P*-wave first-motion picks, a misfit value <0.20, and a station distribution ratio between 0.4 and 0.75. When this ratio has a low value (<0.4), a reasonably large number of the data lie near the nodal planes in the solution, which is a less robust solution compared to the maximum 0.75 where the stations are uniformly distributed surrounding the fault trace. Finally, the uncertainty for the strike, dip, and rake is $<30°$. We compute distance, azimuthal angle, and takeoff angle with the Hypoinverse algorithm (Klein, 2002) using fixed event locations and the same velocity model used in HYPODD, as neither HYPODD nor

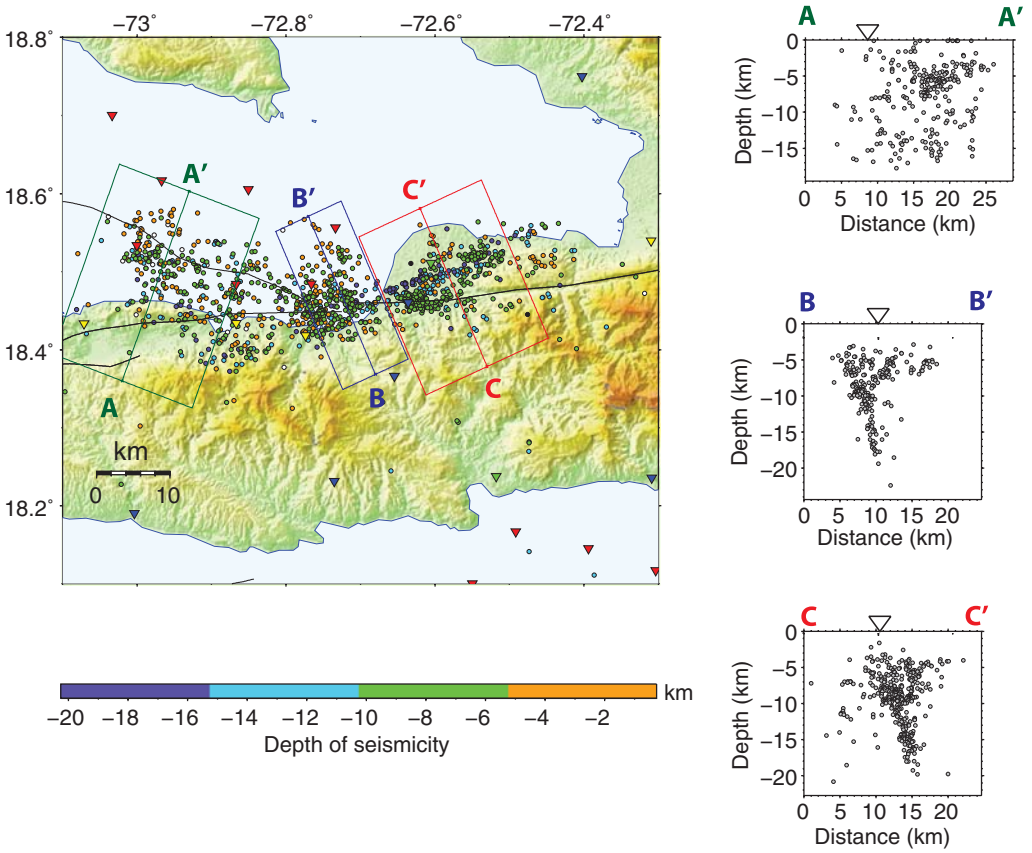

Figure 8. Aftershock locations from VELEST for 1274 events from the final 1D velocity inversion with station corrections. Seismic stations, triangles. Clusters of hypocenters within the rectangular boxes are included in the corresponding cross sections and are referred to in the text as clusters A, B, and C, respectively . The open triangles in the cross sections indicate the surface trace of the Enriquillo fault at the center of the rectangular box.

VELEST outputs takeoff angle. Our final dataset contains focal mechanisms for 109 earthquakes, which are shown in Figure 12 (for a complete list of focal mechanisms, Ⓔ see Table S3 in the supplement). The mechanisms are sorted based on the plunge of their principal stresses.

Results

Fault Geometry from Relocated Aftershocks

The relative aftershock relocations from HYPODD are more tightly clustered (Fig. 9) than the absolute VELEST locations (Fig. 8). We show several cross sections in Figure 9 to illustrate the geometry of the three distinct clusters in the aftershock zone. We determine the cross-section orientation that minimizes the dispersion of the locations for each structure from a single plane. The hypocentral errors (400 m horizontal and 1 km vertical) are smaller than the width of the linear features evident on these cross sections. The aftershocks located in zone B, which strike N85 ± 12°E, clearly delineate a planar structure dipping ~71° to the north. Considering the hypocentral errors and the width of the dipping feature, we estimate the error on the fault dip to be ±2°. Zone C has an orientation slightly different from that of zone B (N68° ± 7°E) and dips less steeply (65° ± 1°NW).

These two zones, B and C, correlate with the two main patches of coseismic slip on the Léogâne fault found in the geodetic and seismic finite fault slip inversions (Calais *et al.*, 2010; Hayes *et al.*, 2010). Although their fault geometry and segmentation is inconsistent with the local geology, Meng *et al.* (2012) also retrieved two major patches of slip that one could say correlate spatially with the other inversions and our two clusters of aftershocks B and C. Aftershocks in zone A delineate a structure above 8 km depth dipping 45° ± 2° to the south, which intersects the surface near the mapped location of the Trois Baies fault. The Trois Baies fault was originally mapped from seafloor bathymetry and shallow seismic chirp profiles that showed discontinuities in recent seafloor sediments (Momplaisir, 1986). Events in zones B and C seem to have their peak in seismicity starting about two months after the mainshock. The western aftershocks from zone A and part of zone B started almost instantaneously, however, which suggests that these events were triggered indirectly by stress changes due to the mainshock

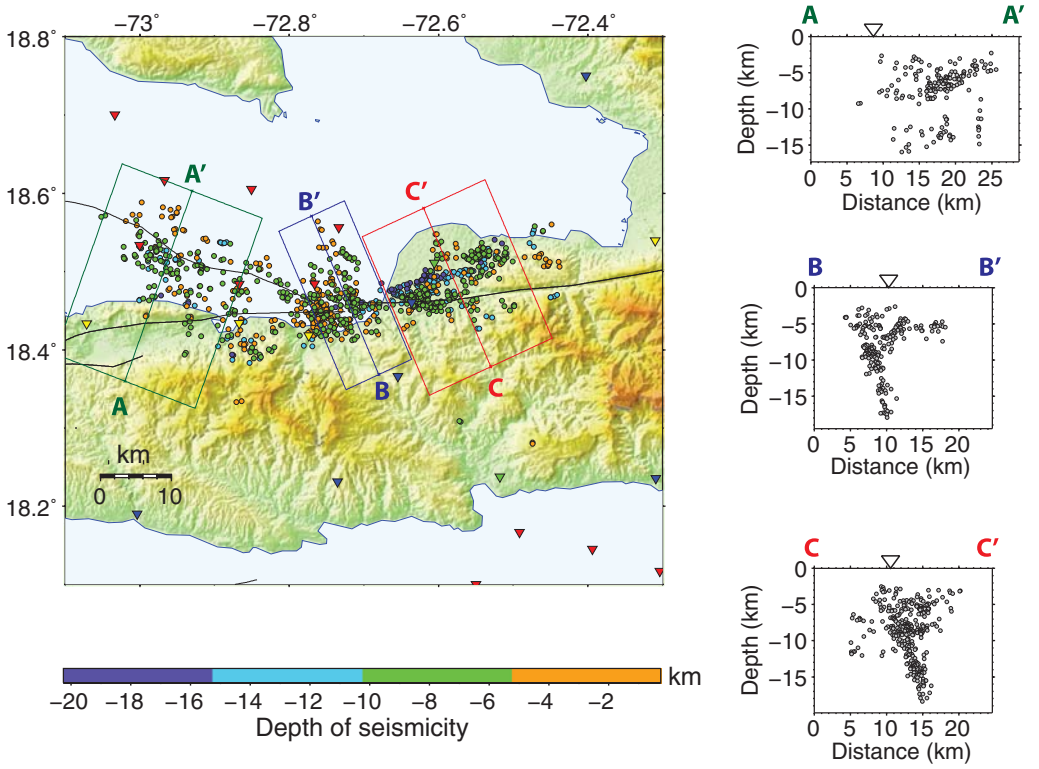

Figure 9. Final double-difference aftershock locations for 1023 events using HYPODD with LSQR. Seismic stations, triangles. Hypocenters within the rectangular boxes are included in the corresponding cross section. The open triangles in the cross sections indicate the surface trace of the Enriquillo fault at the center of the rectangular box.

rather than readjustment of stresses on the fault plane itself (Fig. 13). This assumption is in agreement with the fact that the western aftershocks in zone A occurred in a region where no slip was shown in the fault rupture models (e.g., Calais *et al.*, 2010; Hayes *et al.*, 2010). In addition, the calculation of Coulomb stress changes caused by the coseismic rupture (Symithe *et al.*, 2013) shows that these earthquakes occur in a region of increased stress. Care should be taken in the

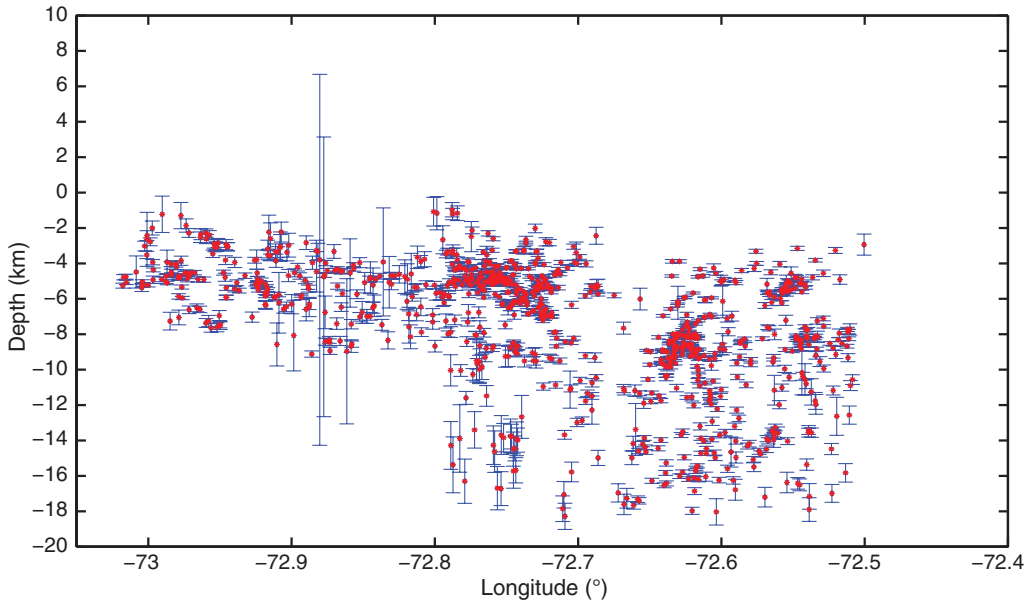

Figure 10. Vertical error calculated for 923 events using HYPODD with SVD. Horizontal error bars (not shown) are 400 m and vertical errors are 1 km excluding the events in the Trois Baies cluster at approximately −72.9, which are poorly constrained in depth (see text).

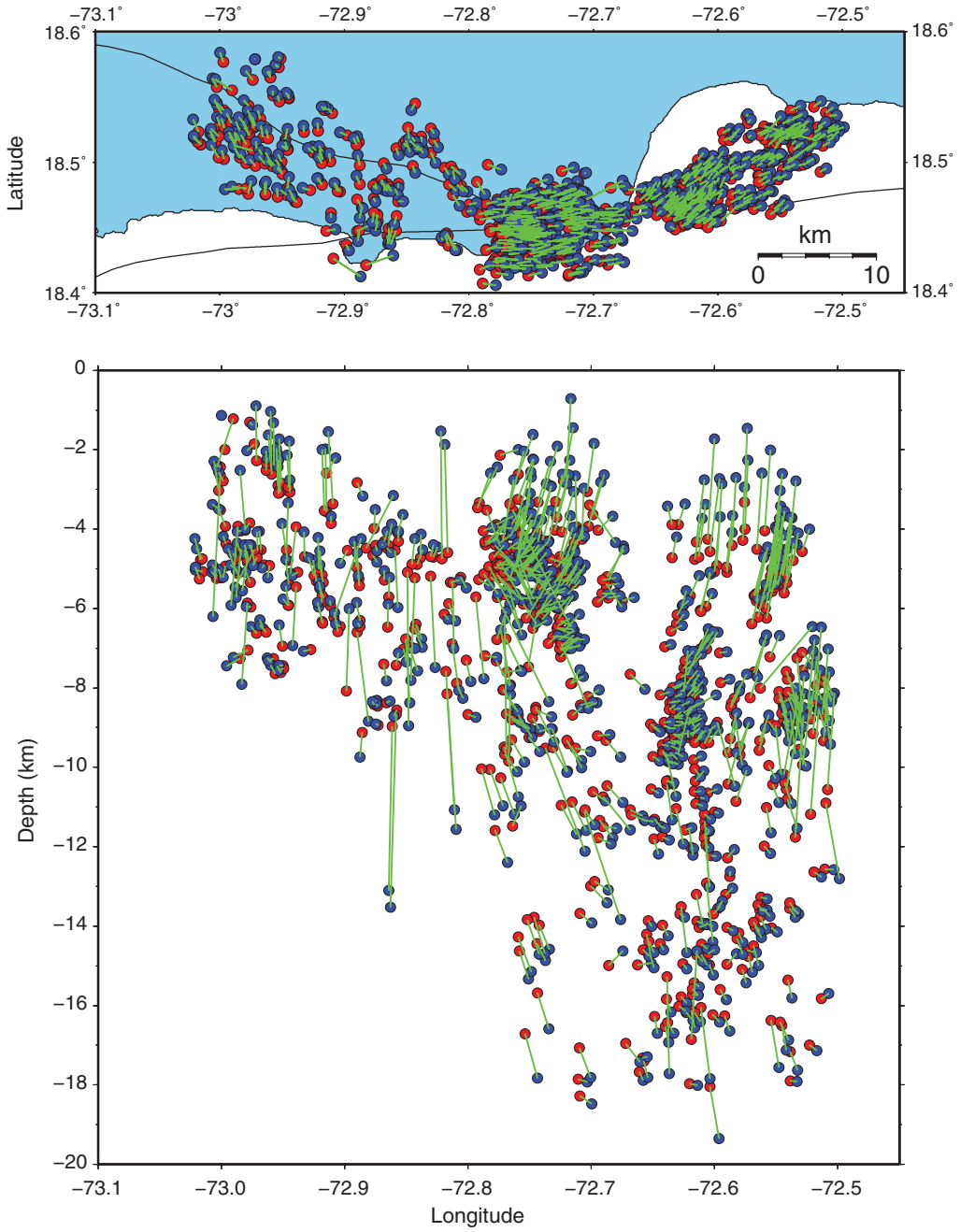

Figure 11. Sensitivity test for three subsets of locations, comparing the LSQR results from HYPODD (blue circles) and SVD results (red circles). Offsets between the two solutions are also indicated (green lines). Locations of two deep events in the western zone, shown by the large vertical offset between the two estimates, are poorly constrained.

interpretation of the time sequence of aftershock occurrence because of the changes in the recording network and some technical problems in the data during the period when the micro-OBS were retrieved (Fig. 13).

Shallow aftershocks (above 10 km) in cross sections B–B′ and in C–C′ on the north side of the Léogâne fault plane appear to be on one or more shallow south-dipping fault planes (Fig. 9). The depth errors of these shallow aftershocks are smaller than the variation of the locations from a single plane, giving confidence to the argument that they may be delineating antithetic fault features in the hanging-wall block. In cluster B the dip of this shallow south-dipping structure is oriented closer to the strike of the Trois Baies fault. Note that although there is some ambiguity in cluster B, the shallow south-dipping events in cluster C are clearly not parallel to the south-dipping Trois Baies fault.

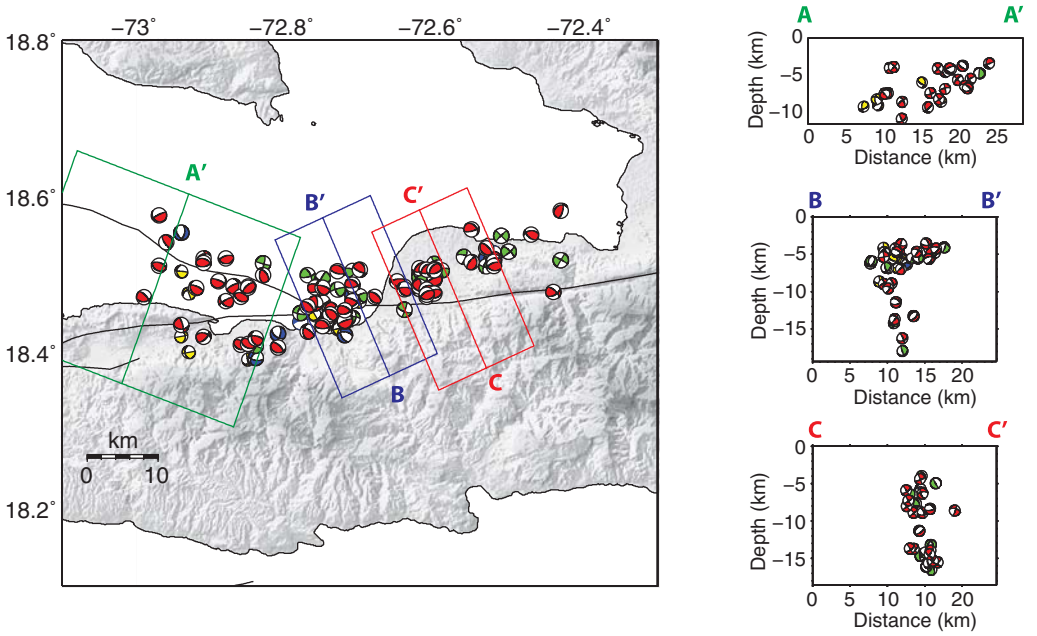

Figure 12. First-motion focal mechanisms from FPFIT for 109 events composed of 9 normal mechanisms (blue), 28 strike-slip mechanisms (green), 60 thrust mechanisms (red), and 12 other oblique mechanisms (yellow). Focal mechanisms within the rectangular boxes are included in the corresponding cross section. Cross sections present a vertical cross-sectional view of the focal planes.

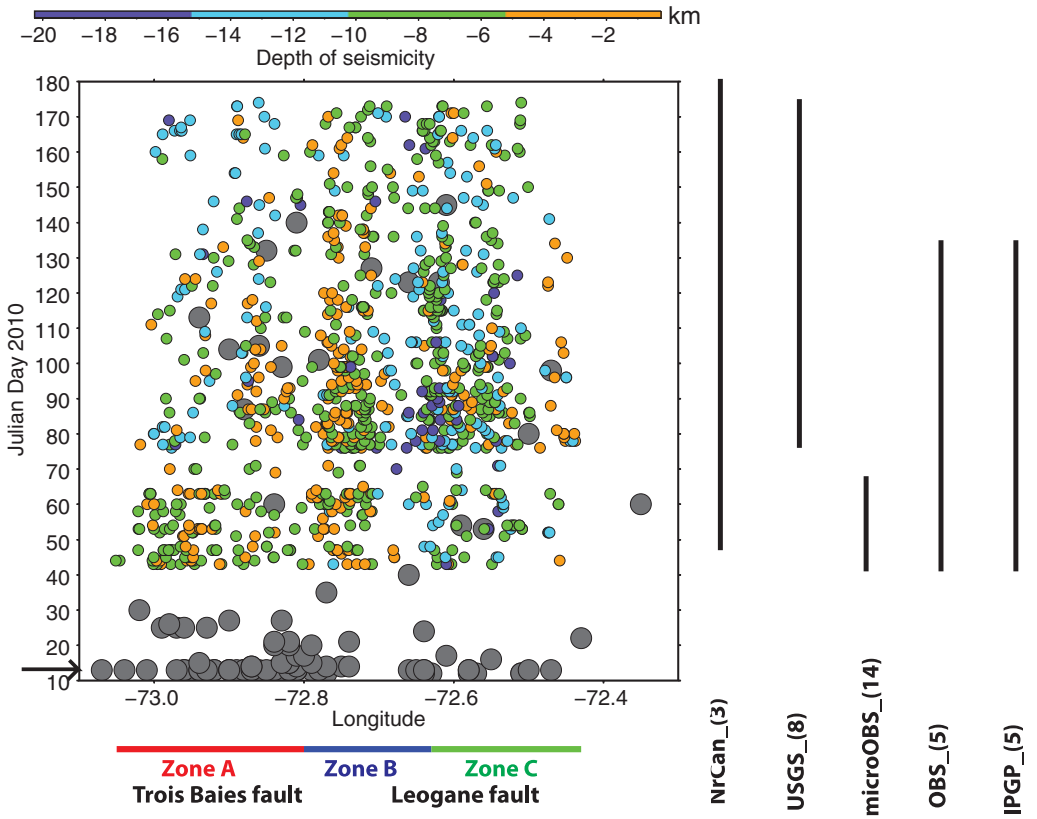

Figure 13. Distribution of the aftershocks as a function of time and longitude, approximately parallel to the Enriquillo fault. The gray circles indicate the events from the National Earthquake Information Center (NEIC) catalog, and the others are the events from this study. The gap between days 66–75 is due to technical problems. Bars on the right show the time period when each subset of seismometers was deployed. Day of the mainshock, black arrows.

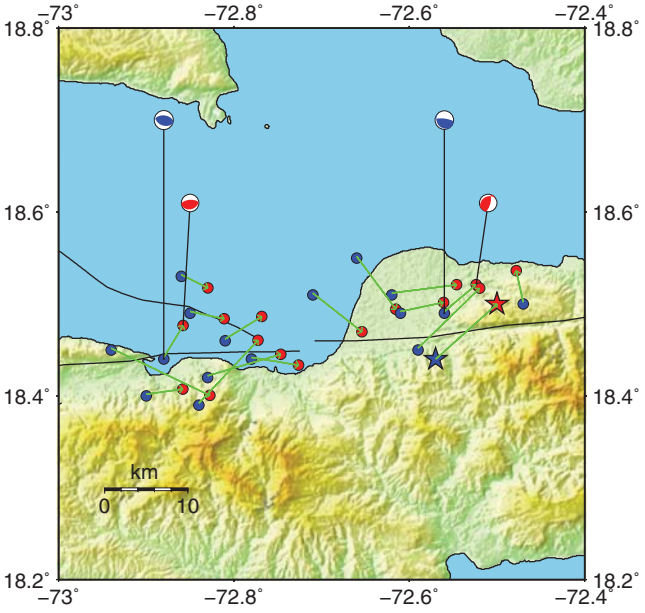

Figure 14. Comparison of relocated hypocenters (red circles) and National Earthquake Information Center (NEIC) locations (blue circles). The location of the mainshock (red star), is estimated by offsetting the NEIC location by the average offset of the aftershocks for which solutions can be compared. Blue focal mechanisms are from Nettles and Hjörleifsdóttir (2010); red are from this study.

Focal Mechanism Constraints on Fault Geometry

The focal mechanism nodal planes from zone A of Figure 12 show south-dipping thrust events that are consistent with the shallowly dipping Trois Baies fault structure. The mechanisms of events in zone B are thrust and strike slip. Primarily strike-slip motion was found in the coseismic slip inversion models for the subevent near zone B (e.g., Calais *et al.*, 2010; Hayes *et al.*, 2010). The strike-slip aftershocks have one nodal plane aligned with the direction of the Léogâne fault. Nodal plane orientations of shallow events within the hanging-wall block are not parallel to the deeper fault geometry in the central aftershock cluster B but are, however, aligned with the thrust events in the Trois Baies fault region (zone A). This suggests that the shallow events are responding to stress changes within the rock volume rather than indicating the orientation of the primary mainshock rupture, or that a structure similar to—or continuous with—the Trois Baies thrust extends into this hanging-wall block. Most events of zone C have one nodal plane parallel to the dipping structure shown in Figure 12. In contrast to zones A and B, the thrust mechanisms in this zone are clearly oriented parallel to the Léogâne fault, consistent with the slip directions of the Calais *et al.* (2010) and Hayes *et al.* (2010) inversions on the east part of the rupture. We note that although there is one strike-slip focal mechanism located near the Enriquillo fault trace east of the main rupture, it has neither of its nodal planes parallel to the Enriquillo fault. One of its nodal planes is, however, parallel to the Léogâne fault. Focal mechanisms from 10 to 20 km deep do not provide convincing evidence that the Enriquillo fault was activated in this aftershock sequence. The deeper events, for example on B–B′, show a mixture of strike-slip and thrust mechanisms. We are not able to single out any vertical or subvertical structure with predominantly strike-slip focal mechanisms that would correspond to the Enriquillo fault.

Discussion

Possible Shift of the Mainshock Location

We compare aftershock locations from the National Earthquake Information Center (NEIC) catalog with the corresponding events from this new dataset of precisely relocated events (Fig. 9). We find an average offset of ∼10 km, with relocated aftershocks from this study shifted to the northeast of their NEIC catalog locations. This relatively large offset could be explained by the lack of nearby stations that were available for the routine teleseismic locations for this oceanic island environment and the corresponding uncertainty in the shallow velocity structure. This suggests that the NEIC mainshock location should also be shifted by a similar amount. This shift would move the mainshock away from the Enriquillo fault and put it on the north-dipping fault on the C–C′ cross section of Figure 9, that is to say, on the Léogâne fault. We also compare the moment tensor focal mechanisms from Nettles and Hjörleifsdóttir (2010) and the matching events of the new focal mechanism dataset (Fig. 14). To the west, only one event is common between the two datasets, with similar mechanisms for both studies. In the east, there is also one common event, but the mechanisms differ. The mechanism from Nettles and Hjörleifsdóttir (2010) does not match the trend delineated by the aftershocks, but the one from this study does show a correlation with the aftershock trend. If we assume the locations for the western events of Nettles and Hjörleifsdóttir (2010) are occurring on the same structures as our relocated thrust events from zone A, this suggests that the larger aftershocks, including an M_w 6.0 aftershock 10 days after the main event, most likely occurred on the shallowly dipping Trois Baies reverse fault.

The aftershock relocations and focal mechanism from this study can also be compared to the results from de Lépinay *et al.* (2011), when a smaller subset of stations was available. They relocated 130 aftershocks using only the OBS stations and the five stations from IPGP, and only for the time period from 14 February to 1 March 2010. Their results clearly show seismicity near the Trois Baies fault but not the details of the dip of this fault and the structures in zone B and C of this study. Also, their regional waveform inversion results for 12 events in January reveal that 7 early events associated with zone A of this study (Fig. 12) were pure thrust. The strike, dip, and rake from all of those seven events are in good agreement with the pure thrust mechanisms found in this study. Nettles and Hjörleifsdóttir (2010) and de Lépinay *et al.* (2011) clearly show the preponderance of large early

aftershocks with thrust mechanisms, and our precise locations and similarity of focal mechanisms allow us to infer that these large early events were triggered on the Trois Baies fault structure. This also implies that the Trois Baies fault should be considered an active fault, with its own contribution to seismic hazard in the region, and that perhaps other offshore thrusts contribute as well.

Overlapping Structures

The aftershock distribution forms a complex zone of faulting from 3 to 18 km depth (Fig. 9). The majority of aftershocks fall on a north-dipping fault plane, now referred to as the Léogâne fault. The A–A′ cross section shows a south-dipping fault plane that we associate with the Trois Baies fault. The fault zone is particularly complicated at B–B′, at the intersection of the Trois Baies, Enriquillo, and Léogâne faults. At this location, the Léogane fault is clearly seen in the seismicity cross section from 5 to 18 km, and the rest of the aftershocks appear to lie on subparallel south-dipping antithetic fault planes. The thrust focal mechanisms of these shallow events are parallel to those in the A–A′ Trois Baies cluster, so some subsets may be indicating the continuation of the Trois Baies fault. In the C–C′ cross section, the Léogane fault is seen with the shallowest earthquakes at ~5 km depth at the trace of the Enriquillo. The shallow aftershocks on the north side of the fault once again appear to occur on antithetic south-dipping fault planes, but here the focal mechanisms are parallel to the strike of the Léogâne fault, not the Trois Baies fault.

The 1989 Loma Prieta and 2003 San Simeon earthquakes are other examples of events that produced complicated aftershock patterns after dip-slip or thrust events in a primarily strike-slip tectonic environment. The Loma Prieta event was associated with a steeply dipping thrust fault near the San Andreas and produced aftershocks with a great diversity of mechanisms (Dietz and Ellsworth, 1990; Beroza, 1991; Kilb *et al.*, 1997). Precise relocations for that aftershock sequence indicate that shallow events (above 6 km depth) occurred on a variety of en-echelon planes above the edge of the buried thrust fault (Twiss and Unruh, 2007). The main rupture of the San Simeon event occurred on the Oceanic thrust fault, between the strike-slip San Gregorio–Hosgri fault zone and the Rinconada fault, west of the main trace of the San Andreas in the Coast Ranges. Along the length of the main rupture, cross sections show several different expressions of antithetic fault planes producing aftershocks in the 6–10 km depth range (McLaren *et al.*, 2008).

We propose that in Haiti, similar to the inferences for the Loma Prieta earthquake, the tightly aligned aftershocks illuminate a steeply dipping mainshock rupture plane and the shallow aftershocks reflect activity above some transition depth where lower confining stress allows them to occur on any fault plane accommodating strike slip with a compressional component. This proposed solution may be more favorable in regions where the near-surface material is

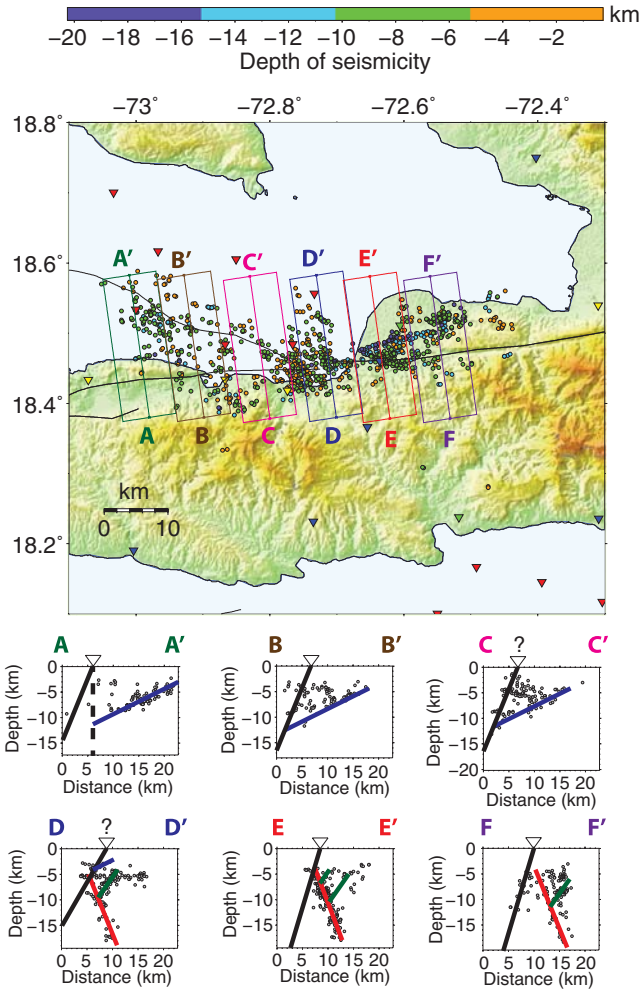

Figure 15. Cross sections perpendicular to the Enriquillo fault illustrating possible fault structures. Hypocenters within the rectangular boxes are included in the corresponding cross section. The open triangles in the cross sections indicate the surface trace of the Enriquillo fault. The red line shows the main earthquake rupture on the Léogâne fault; blue lines show the Trois Baies thrust fault; green lines show south-dipping antithetic structures delineated by aftershocks possibly triggered by Coulomb stress changes following the mainshock. The black lines in the cross sections show the hypothesized location of the Enriquillo fault, which is believed to dip from 65° north (Prentice *et al.*, 2010) to vertical.

weaker and can result in deformation on faults surrounding the Enriquillo in a flower structure. Figure 15 shows several cross sections perpendicular to the Enriquillo fault that illustrate where the aftershock structures intersect the supposed Enriquillo fault plane. In this figure, we removed the events that were not well constrained and we assumed a south-dipping Enriquillo fault as it agrees best with the aftershock patterns, as well as the geological observations at the surface (Prentice *et al.*, 2010). In Figure 15, cross sections A–A′ and B–B′, the Enriquillo fault is onshore and mapped with confidence at the surface. In cross section C–C′, however, the exact trace of the continuation of the Enriquillo fault

is unidentified offshore. Here, the aftershocks are restricted to the Trois Baies fault and are limited to the north side of the surface trace of the Enriquillo fault. In cross sections D–D′, the offshore part of the Enriquillo fault is also poorly known. Here, the aftershocks following the main Léogâne fault appear to be limited by a south-dipping Enriquillo fault. Furthermore, the aftershocks tend to delineate two distinct south-dipping structures: a shallower fault plane above 5 km depth, which may be the continuation of the Trois Baies fault, and a steeper south-dipping fault plane that we assume to be an antithetic fault. Near the cross-sections E–E′ and F–F′, the Enriquillo fault trace is clearly seen in the topography and has been mapped on land (Prentice *et al.*, 2010). Here, the aftershocks occurred on the Léogâne fault plane, which is clearly on the north side of the Enriquillo fault trace, and on a set of antithetic fault structures, which are similar to the patterns seen in Loma Prieta. Note that in cross section F–F′, and possibly in cross section C–C′, there are some events located where we would expect to see a hypothetical south-dipping Enriquillo fault. Unfortunately, these events are not large enough to be able to calculate focal mechanisms to determine if they are consistent with strike-slip motion on the Enriquillo fault.

Farther east of cross section F–F′, the surface geology surrounding the Enriquillo fault changes to Eocene pelagic limestones that form the high ridge topography. The southward dip on the Enriquillo fault (Prentice *et al.*, 2010) would lead to the uplifted topography south of the fault over geologic time. We hypothesize that the presence of competent material in the upper kilometers of the crust could have been a factor in this particular earthquake favoring rupture on the Léogâne fault where the dip-slip antithetic faulting occurs in other, possibly weaker, geologic materials. These hypotheses for the relationship between fault geometry and aftershock occurrence could be tested by using the entire aftershock focal mechanism dataset to determine the best-fitting background stress field as was done for Loma Prieta and other earthquakes (Beroza, 1991; Kilb *et al.*, 1997; Hardebeck, 2010).

Relative Location Errors

Earthquake locations calculated assuming a 1D velocity structure in the presence of significant lateral velocity variations tend to be biased in a direction away from regions of high-velocity anomalies. The important question to consider is whether the aftershocks in cluster B that in map view appear to be south of the Enriquillo fault would move north if located in a 3D model. In synthetic local earthquake tomography tests, the location biases are on the order of 1–1.5 (Zhang and Thurber, 2003). One might expect that the locations of events in the Trois Baies cluster A and cluster B might be biased toward the southeast because of the anomalously large residuals at stations on the south side of the peninsula (i.e., HA01, HA03). The stations directly south of this cluster, however, in particular station GRG, have no large residuals, and no systematic variation of residuals with azimuth, so that would limit that effect.

The HYPODD hypocenters more sharply define linear features in the seismicity because they remove the scatter from systematically biased station residuals due to unmodeled velocity variations outside the source region (Waldhauser and Ellsworth, 2000; Hardebeck, 2010). Master event location techniques do not provide reliable absolute locations because they are calculated relative to a master event, the location of which may be biased. HYPODD, however, solves for the best-fitting centroid of the cluster as well as the offset of each hypocenter from the centroid, allowing the hypocenters to be put in an absolute reference frame. That aspect is discussed by Menke and Schaff (2004) where they have demonstrated the sensitivity of differenced travel times to absolute locations. Alternate techniques such as the source specific station correction method (Richards-Dinger and Shearer, 2000) are advantageous in extended regions where earthquake hypocenters are not confined to a small region and provide comparable location accuracy to HYPODD but would not provide an improvement when the source region is limited, as in this case.

Many local earthquake tomography studies have estimated the bias in locations calculated in a 1D velocity model compared to 3D locations. For example, 3D velocity variations in the LA basin were shown to bias 1D locations up to 2 km (Hauksson and Haase, 1997). A study on the San Jacinto fault zone in southern California compared 3D locations, relative locations, and 1D locations and found the 1D locations biased by 700 m compared to the 3D locations, but the offsets of relative locations in a 1D model relative to 3D locations were not systematic and < 200 m (Scott, 1992). HYPODD locations in a 1D model at Parkfield (Waldhauser *et al.*, 2004) have horizontal errors < 200 m and image the linear feature of the San Andreas fault remarkably. They have no perceptible bias relative to the mapped fault trace compared to HYPODD locations in a 3D model, and have much less scatter than absolute locations in a 3D model, despite the large velocity contrast at the fault (Thurber *et al.*, 2006). Parkfield has a large contrast not only in the fault zone but also in the basement on opposite sides of the fault. The evidence here for velocity variations does not appear to be any larger than that seen at Parkfield. Therefore, we argue that, without clear systematic variation of residuals in the near source region of the Haiti earthquake, HYPODD locations in a 1D model would be sufficient to resolve the linear features of the fault zone in an absolute sense relative to the mapped fault trace. Nevertheless, we are aware that Michelini and Lomax (2004) have shown a theoretical sensitivity of the shape of relocated clusters, which can modify slightly the dip induced on our figures.

The hinge line of InSAR range changes (Symithe *et al.*, 2013) from uplift to subsidence occurs south of the coastline where the Enriquillo fault trace is postulated to be offshore. Although the plane of the aftershocks is 3 km south of the fault plane found in Calais *et al.* (2010), its location is within

the uncertainties in the slip inversion, and the uplift south of the coastline is consistent with the absolute locations shown in cross section D–D′ of Figure 15. In the worst case where biases reached the level of 1–2 km, the epicenters of events in cluster B would still fall south of the mapped surface trace of the fault and require an interpretation of a south-dipping Enriquillo fault. The conclusions concerning the geometry of the fault would not be altered using a 3D velocity model, although a future tomographic study would provide additional interesting information on the subsurface structure and tectonics.

Relationships to Coseismic Slip Models

All coseismic slip inversions find the same first-order features. They all show that the rupture did not reach the surface, they identify two patches with large slip, and the Léogâne rupture has most of the moment. In Calais *et al.* (2010) and Hayes *et al.* (2010) models, the eastern slip patch shows predominantly reverse dip-slip motion whereas the western patch shows primarily strike-slip motion. This does not entirely correlate with the distribution of focal mechanisms, because the corresponding aftershock zones B and C in this dataset both have primarily thrust mechanisms with fewer strike-slip mechanisms. In the Hayes *et al.* (2010) slip inversion, which included seismological, geodetic, and geologic data from coastal uplift, the rupture started at depth on the Enriquillo fault and triggered rupture of the north-dipping Léogâne fault. Their choice of fault planes assumed the rupture started at the NEIC location of the mainshock. Assuming that this location is biased by 10 km and should in fact be located farther to the northeast, as discussed previously, this implies that the rupture might instead have initiated on the Léogâne fault. Calais *et al.* (2010) used a single fault to model the coseismic slip; there were, however, no relocated aftershocks at the time to constrain the orientation of the fault trace, so it was based on a grid search method for determining the best fault orientation for the spatially variable slip inversion. This result, independent of the aftershock locations shown here, resolved a fault plane with similar strike and dip to the structures seen in these final aftershock relocations.

Recently, two more slip inversions have been published. The slip distribution from de Lépinay *et al.* (2011) is obtained from a joint inversion of InSAR and seismological data and is modeled by a single fault plane, with a combination of reverse and left-lateral strike-slip motion near zone C aftershocks and primarily strike-slip motion near zone B. This motion is consistent with the focal mechanisms of zone C, as both of those zones have primarily thrust and strike-slip mechanisms. Once again, however, it is surprising that the slip near zone B is primarily strike slip when the zone B aftershocks have both thrust and strike-slip mechanisms. The slip distribution from Meng *et al.* (2012) was based on a combination of InSAR, GPS, and teleseismic data. Although their fault geometry and segmentation is inconsistent with geological data and the aftershock relocations found here, Meng *et al.* (2012) also retrieved two major patches of slip that correlate spatially with the other inversions and our two clusters of aftershocks. They investigated the possibility that the mainshock rupture extended to the Trois Baies fault and found slip was confined to <22 km west of the mainshock epicenter and did not extend significantly offshore. However they incorrectly specified the Trois Baies fault with dip to the north. They were most likely imaging slip on the segment of the Léogane fault near B–B′ (Fig. 9) that we found to have slightly different orientation from the Léogane fault near C–C′.

A more robust inversion with all the available data and with fault planes that follow the trends shown in Figure 9 would provide the best possible description of the mainshock rupture. Symithe *et al.* (2013) carried out a coseismic slip inversion similar to Calais *et al.* (2010) but used a rupture geometry constrained by the aftershock relocations determined in this study. They also find two main patches of slip, with larger values than Calais *et al.* (2010), on the patch east of zone C. Consistent with Calais *et al.* (2010), they find a partitioning of coseismic slip with a larger component of strike slip on the western patch than on the eastern patch, which shows mostly thrust motion. As stated previously, we do not see a similar partitioning in the focal mechanisms: both zone C and zone B have primarily thrust events and a smaller number of strike-slip events. If we exclude from zone B shallow events with thrust mechanisms that are oriented parallel to the Trois Baies fault, however, there is a larger proportion of strike-slip events relative to thrust events in zone B than in zone C. Symithe *et al.* (2013) tested the possibility of coseismic slip on the Trois Baies fault in a revised geodetic inversion, with the fault correctly constrained to a southward-dipping plane by the aftershock locations in this study, and confirmed that the geodetic data do not require slip on the Trois Baies fault. A future study that combines the surface deformation observations with the teleseismic data and uses the fault geometry determined in this study could perhaps determine definitively if there was any seismic energy released from the Trois Baies fault at the time of the mainshock.

Conclusions

We use a compilation of data from the temporary seismic stations deployed after the 12 January 2010 Haiti earthquake to obtain high-resolution aftershock relocations with an epicentral error of 400 m and a depth error of the order of 1 km as well as a large set of aftershock focal mechanisms. Cross sections through the aftershock distribution show several dipping fault planes, indicating that the rupture zone of the 2010 Haiti quake was complex. The central and eastern clusters of aftershocks delineate a main north-dipping rupture plane with slightly different dip on the central and eastern segments. These two clusters correlate with the locations of the two main patches of slip determined in the Calais

et al. (2010) source inversion that led to the interpretation of rupture on the previously unknown Léogâne fault, rather than the Enriquillo fault.

To the west, outside of the rupture zone, the aftershocks define a shallow structure dipping to the south that we conclude to be the Trois Baies thrust fault, based on the orientation and sense of the fault planes from the new focal mechanism dataset. This structure has generated a surprisingly large number of aftershocks, as well as the largest magnitude ones. This high level of activity could result from stress triggering caused by the main coseismic rupture (Symithe *et al.*, 2013). Although a small number of aftershock focal mechanisms were strike slip, they occurred within the dipping structures that we associate with the Léogâne fault. There is no clear evidence of a coherent pattern of strike-slip events on a separate vertical or south-dipping Enriquillo fault. This event was unique in the quantity and size of aftershocks that occurred away from the main rupture. There is an indication that aftershock activity on the main Léogane rupture plane peaked two months after the mainshock, although this requires further testing with attention to changes in the deployment geometry. The aftershock mechanisms (primarily thrust) trend differently from what was initially expected based on the predominant strike-slip tectonic style of southern Haiti. Upon re-evaluation, however, it is consistent with the transpressional deformation pattern clearly visible in the older thrust belt geology (Pubellier *et al.*, 2000) and in the interseismic GPS measurements (Calais *et al.*, 2010; Benford *et al.*, 2012).

We derive a 1D crustal *P*- and *S*-wave velocity model through a joint inversion for velocity, hypocenters, and station corrections. Although there is a range of possible models satisfying the data, inversions with different starting models lead to *P*-wave models with velocity of 5.2–5.5 km/s near the surface, steep gradients between the surface and 5 km, a layer from 5 to 10 km depth with velocity of 6.5 km/s, and a higher velocity lower crust of 7.2 km/s. Moho depth and upper mantle velocities are not strongly constrained because most recordings were within an epicentral distance of 60 km; the Moho depth and velocity contrast, however, are consistent with results determined using regional seismic stations (McNamara *et al.*, 2012). The simultaneous inversion also included station corrections that correlate with geologic structure. In particular, large positive *S*-wave station corrections are found for the deep OBS stations, which might be related to extensive thicknesses of low-velocity sediments in the submarine basins that parallel the coastline.

Data and Resources

The USGS and NRCan waveforms can be freely downloaded from the Incorporated Research Institutions for Seismology (IRIS) using http://www.iris.edu/SeismiQuery/breq_fast.htm (last accessed June 2011), and the Geoazur —IPGP waveforms can be requested from Anne Deschamps at deschamps@geoazur.unice.fr (last requested June 2011).

Acknowledgments

This research was supported by Grants from the U.S. National Science Foundation (awards EAR-0409487, EAR-RAPID-1024990, and EAR-1045809 to Eric Calais). Steeve J. Symithe and Roby Douilly are supported by a training grant from the Voilà Foundation (Trilogy International), which we thank for their commitment to improving higher education in Haiti. We thank the Haiti Bureau of Mines and Energy and the Faculty of Science of the University of the State of Haiti for their support to our work in Haiti. We thank the support of INSU/CNRS, IRD, and IFREMER, which allowed the Haiti OBS cruise, and the INSU "Aléas et risques" program, which supported the aftershocks analysis. We acknowledge the benefit of discussions with Robert L. Nowack, Carol Prentice, Walter Mooney, Andrew M. Freed, and Roberte Bien-Aimé Momplaisir, which significantly improved this work.

References

Ali, S. T., A. M. Freed, E. Calais, D. M. Manaker, and W. R. McCann (2008). Coulomb stress evolution in Northeastern Caribbean over the past 250 years due to coseismic, postseismic and interseismic deformation, *Geophys. J. Int.* **174,** 904–918.

Altidor, J., A. Dieuseul, W. Ellsworth, D. Given, S. Hough, M. Janvier, J. Maharrey, M. Meremonte, B. Mildor, C. Prepetit, and A. Yong (2010). Seismic monitoring and post-seismic investigations following the 12 January 2010 M_w 7.0 Haiti earthquake, *AGU Fall Meeting Abstracts*, abstract #U11A-07, Vol. **1**, 8.

Bakun, W. H., C. H. Flores, and S. Uri (2012). Significant earthquakes on the Enriquillo fault system, Hispaniola, 1500–2010: Implications for seismic hazard, *Bull. Seismol. Soc. Am.* **102,** 18–30.

Benford, B., C. DeMets, and E. Calais (2012). GPS estimates of microplate motions, northern Caribbean: Evidence for a Hispaniola microplate and implications for earthquake hazard, *Geophys. J. Int.* **191,** 481–490, doi: 10.1111/j.1365-246X.2012.05662.x.

Beroza, G. C. (1991). Near-source modeling of the Loma Prieta earthquake: Evidence for heterogeneous slip and implications for earthquake hazard, *Bull. Seismol. Soc. Am.* **81,** 1603–1621.

Calais, E., A. Freed, G. Mattioli, F. Amelung, S. Jónsson, P. Jansma, S. H. Hong, T. Dixon, C. Prépetit, and R. Momplaisir (2010). Transpressional rupture of an unmapped fault during the 2010 Haiti earthquake, *Nat. Geosci.* **3,** 794–799.

Calais, E., Y. Mazabraud, B. Mercier de Lépinay, P. Mann, G. Mattioli, and P. Jansma (2002). Strain partitioning and fault slip rates in the northeastern Caribbean from GPS measurements, *Geophys. Res. Int.* **29,** 3-1–3-4.

Christensen, N. I. (1996). Poisson's ratio and crustal seismology, *J. Geophys. Res.* **101,** 3139–3156.

Courboulex, F., J. L. Berenguer, A. Tocheport, M. P. Bouin, E. Calais, Y. Esnault, C. Larroque, G. Nolet, and J. Virieux (2012). Sismos à l'Ecole: A worldwide network of real-time seismometers in schools, *Seismol. Res. Lett.* **83,** no. 5, 870–873.

Crosson, R. S. (1976). Crustal structure modeling of earthquake data 1. Simultaneous least squares estimation of hypocenter and velocity parameters, *J. Geophys. Res.* **81,** 3036–3046.

de Lépinay, B. M., A. Deschamps, F. Klingelhoefer, Y. Mazabraud, B. Delouis, V. Clouard, Y. Hello, J. Crozon, B. Marcaillou, D. Graindorge, M. Vallée, J. Perrot, M.-P. Bouin, J.-M. Saurel, P. Charvis, and M. St-Louis (2011). The 2010 Haiti earthquake: A complex fault pattern constrained by seismologic and tectonic observations, *Geophys. Res. Lett.* **38,** L22305.

DeMets, C., D. F. A. Gordon, D. Argus, and S. Stein (1994). Effect of recent revisions to the geomagnetic reversal timescale on estimates of current plate motions, *Geophys. Res. Lett.* **21,** 2191–2194.

Dietz, L. D., and W. L. Ellsworth (1990). The October 17, 1989, Loma Prieta, California, earthquake and its aftershocks: Geometry of the sequence from high-resolution locations, *Geophys. Res. Lett.* **17,** 1417–1420.

Frankel, A., S. Harmsen, C. Mueller, E. Calais, and J. S. Haase (2011). Initial seismic hazard maps for Haiti, *Earthq. Spectra* **27,** S23–S41.

Goldstein, P., D. Dodge, M. Firpo, and L. Minner (2003). 85.5 SAC2000: Signal processing and analysis tools for seismologists and engineers, *Int. Geophys.* **81,** 1613–1614.

Hardebeck, J. L. (2010). Seismotectonics and fault structure of the California central coast, *Bull. Seismol. Soc. Am.* **100,** 1031–1050.

Hauksson, E., and J. S. Haase (1997). Three-dimensional V_P and V_P/V_S velocity models of the Los Angeles basin and central Transverse Ranges, California, *J. Geophys. Res.* **102,** 5423–5453.

Hayes, G., R. Briggs, A. Sladen, E. Fielding, C. Prentice, K. Hudnut, P. Mann, F. Taylor, A. Crone, R. Gold, T. Ito, and M. Simons (2010). Complex rupture during the 12 January 2010 Haiti earthquake, *Nat. Geosci.* **3,** 800–805.

Helmstetter, A., and D. Sornette (2002). Subcritical and supercritical regimes in epidemic models of earthquake aftershocks, *J. Geophys. Res.* **107,** 1–21.

Hough, S. E., J. R. Altidor, D. Anglade, D. Given, M. G. Janvier, J. Z. Maharrey, M. Meremonte, B. S. L. Mildor, C. Prepetit, and A. Yong (2010). Localized damage caused by topographic amplification during the 2010 M 7.0 Haiti earthquake, *Nat. Geosci.* **3,** 778–782.

Kilb, D., M. Ellis, J. Gomberg, and S. Davis (1997). On the origin of diverse aftershock mechanisms following the 1989 Loma Prieta earthquake, *Geophys. J. Int.* **128,** 557–570.

Kissling, E. (1988). Geotomography with local earthquake data, *Rev. Geophys.* **26,** 659–698.

Kissling, E., W. Ellsworth, D. Eberhart-Phillips, and U. Kradolfer (1994). Initial reference models in local earthquake tomography, *J. Geophys. Res.* **99,** 19,635–19,646.

Kissling, E., U. Kradolfer, and H. Maurer (1995). Program VELEST USERS GUIDE-Short Introduction, Institute of Geophysics, ETH Zurich.

Klein, F. W. (2002). User's Guide to HYPOINVERSE-2000: A Fortran program to solve for earthquake locations and magnitudes HYPOINVERSE: users guide to version 1, 2, 3, and 4, *U.S. Geol. Surv. Open-File Rept. 02-171*.

Manaker, D., E. Calais, A. Freed, S. Ali, P. Przybylski, G. Mattioli, P. Jansma, C. Prépetit, and J. De Chabalier (2008). Interseismic plate coupling and strain partitioning in the northeastern Caribbean, *Geophys. J. Int.* **174,** 889–903.

Mann, P., E. Calais, J. C. Ruegg, C. DeMets, P. E. Jansma, and G. S. Mattioli (2002). Oblique collision in the northeastern Caribbean from GPS measurements and geological observations, *Tectonics* **21,** 1057.

Mann, P., G. Draper, and J. F. Lewis (1991). Geologic and tectonic development of the North America-Caribbean plate boundary in Hispaniola, *Spec. Pap. Geol. Soc. Am.* **262,** 1–28.

McLaren, M. K., J. L. Hardebeck, N. van der Elst, J. R. Unruh, G. W. Bawden, and J. L. Blair (2008). Complex faulting associated with the 22 December 2003 M_w 6.5 San Simeon, California, earthquake, aftershocks, and postseismic surface deformation, *Bull. Seismol. Soc. Am.* **98,** 1659–1680.

McNamara, M., M. Meremonte, J. Z. Maharrey, J. R. Altidor, D. Anglade, S. E. Hough, D. Given, L. G. Benz, and A. Frankel (2012). Frequency-dependent seismic attenuation within the Hispaniola island region of the Caribbean sea, *Bull. Seismol. Soc. Am.* **102,** 773–782.

Mendoza, C., and S. H. Hartzell (1988). Aftershock patterns and main shock faulting, *Bull. Seismol. Soc. Am.* **78,** 1438–1449.

Meng, L., J. P. Ampuero, A. Sladen, and H. Rendon (2012). High-resolution backprojection at regional distance: application to the Haiti *M* 7. 0 earthquake and comparisons with finite source studies, *J. Geophys. Res.* **117,** B04313.

Menke, W., and D. Schaff (2004). Absolute earthquake locations with differential data, *Bull. Seismol. Soc. Am.* **94,** 2254–2264.

Michelini, A., and A. Lomax (2004). The effect of velocity structure errors on double-difference earthquake location, *Geophys. Res. Lett.* **31,** L09602, doi: 10.1029/2004GL019682.

Momplaisir, R. B.-A. (1986). Contribution a l'Etude Geologique de la partie orientale du massif de la hotte (presqu'ile de sud d'Haiti): Synthese structurale des marges de la presqu'ile a partir de donnees sismiques, *Ph.D. thesis*, Univ. Pierre-et-Marie-Curie (Paris VI), Paris, 210 pp.

Moreno, B., M. Grandison, and K. Atakan (2002). Crustal velocity model along the southern Cuban margin: Implications for the tectonic regime at an active plate boundary, *Geophys. J. Int.* **151,** 632–645.

Murphy, A. J., and W. R. McCann (1979). Preliminary results from a new seismic network in the northeastern Caribbean, *Bull. Seismol. Soc. Am.* **69,** 1497–1513.

Nettles, M., and V. Hjörleifsdóttir (2010). Earthquake source parameters for the 2010 January Haiti main shock and aftershock sequence, *Geophys. J. Int.* **183,** 375–380.

Paige, C. C., and M. A. Saunders (1982). LSQR: An algorithm for sparse linear equations and sparse least squares, *ACM Trans. Math. Software (TOMS)* **8,** 43–71.

Perfit, M. R., and B. C. Heezen (1978). The geology and evolution of the Cayman Trench, *Geol. Soc. Am. Bull.* **89,** 1155–1174.

Prentice, C., P. Mann, A. Crone, R. Gold, K. Hudnut, R. Briggs, R. Koehler, and P. Jean (2010). Seismic hazard of the Enriquillo-Plantain Garden fault in Haiti inferred from palaeoseismology, *Nat. Geosci.* **3,** 789–793.

Pubellier, M., A. Mauffret, S. Leroy, J. M. Vila, and H. Amilcar (2000). Plate boundary readjustment in oblique convergence: Example of the Neogene of Hispaniola, Greater Antilles, *Tectonics* **19,** 630–648.

Ratchkovski, N. A., S. Wiemer, and R. A. Hansen (2004). Seismotectonics of the central Denali fault, Alaska, and the 2002 Denali fault earthquake sequence, *Bull. Seismol. Soc. Am.* **94,** S156–S174.

Reasenberg, P., D. Oppenheimer, and USGS (1985). FPFIT, FPPLOT, and FPPAGE: Fortran computer programs for calculating and displaying earthquake fault-plane solutions, *U.S. Geol. Surv. Open-File Rept. 85-739*.

Richards-Dinger, K. B., and P. M. Shearer (2000). Earthquake locations in southern California obtained using source-specific stations terms, *J. Geophys. Res.* **105,** 10,939–10,960.

Scott, J. S. (1992). Microearthquake studies in the Anza seismic gap, *Ph.D. thesis*, University of Calif. San Diego, Scripps Institute of Oceanography, La Jolla, California, 277 pp.

Symithe, S. J., E. Calais, S. J. Haase, A. M. Freed, and R. Douilly (2013). Coseismic slip distribution of the M 7.0 Haiti earthquake and resulting stress changes on regional faults, *Bull. Seismol. Soc. Am.* **103,** no. 4, doi: 10.1785/0120120306.

Thurber, C., H. Zhang, F. Waldhauser, J. Hardebeck, A. Michael, and D. Eberhart-Phillips (2006). Three-dimensional compressional wavespeed model, earthquake relocations, and focal mechanisms for the Parkfield, California, region, *Bull. Seismol. Soc. Am.* **96,** S38–S49.

Twiss, R. J., and J. R. Unruh (2007). Structure, deformation, and strength of the Loma Prieta fault, northern California, USA, as inferred from the 1989–1990 Loma Prieta aftershock sequence, *Geol. Soc. Am. Bull.* **119,** 1079–1106.

Waldhauser, F. (2001). hypoDD- A program to compute double-difference hypocenter locations (hypoDD version 1.0-03/2001), *U.S. Geol. Surv. Open-File Rept. 01-113*.

Waldhauser, F., and W. L. Ellsworth (2000). A double-difference earthquake location algorithm: Method and application to the northern Hayward fault, California, *Bull. Seismol. Soc. Am.* **90,** 1353–1368.

Waldhauser, F., W. L. Ellsworth, D. P. Schaff, and A. Cole (2004). Streaks, multiplets, and holes: high-resolution spatio-temporal behavior of Parkfield seismicity, *Geophys. Res. Lett.* **31,** L18608.

Wiggins-Grandison, M. D. (2004). Simultaneous inversion for local earthquake hypocentres, station corrections and 1-D velocity model of the Jamaican crust, *Earth Planet. Sci. Lett.* **224,** 229–240.

Zhang, H., and C. H. Thurber (2003). Double-difference tomography: The method and its application to the Hayward fault, California, *Bull. Seismol. Soc. Am.* **93,** 1875–1889.

Purdue University
Department of Earth
Atmospheric and Planetary Sciences
West Lafayette, Indiana 47907
rdouilly@purdue.edu
ssymithe@purdue.edu
(R.D., S.J.S.)

Scripps Institution of Oceanography
University of California, San Diego
La Jolla, California 92093
jhaase@ucsd.edu
(J.S.H.)

United States Geological Survey
Menlo Park, California 94025
ellsworth@usgs.gov
(W.L.E.)

Observatoire Volocanologique et Sismologique de Guadeloupe
Institut de Physique du Globe de Paris
97113 Gourbeyre, Guadeloupe
bouin@ipgp.fr
(M.-P.B.)

Ecole Normale Supérieure
Department of Geosciences
UMR CNRS 8538
75231 Paris cedex 5, France
ecalais@geologie.ens.fr
(E.C.)

Lamont Doherty Earth Observatory
Palisades, New York 10964
armb@ldeo.columbia.edu
(J.G.A.)

Géoazur/CNRS
Université de Nice
06560 Sophia Antipolis, France
mercier@geoazur.unice.fr
deschamps@geoazur.unice.fr
(B.M.d., A.D.)

Bureau des Mines et de L'Energie
Port-au-Prince, Delmas, Haiti
saintmildor1953@yahoo.fr
(S.-L.M.)

U.S. Geological Survey
Golden, Colorado 80401
meremonte@usgs.gov
(M.E.M.)

U.S. Geological Survey
Pasadena, California 91106
hough@usgs.gov
(S.E.H.)

Manuscript received 4 October 2012